Journal of Materials Chemistry A

ROYAL SOCIETY OF CHEMISTRY

REVIEW

View Article Online
View Journal | View Issue

Cite this: J. Mater. Chem. A, 2023, 11, 3789

Low-cobalt active cathode materials for high-performance lithium-ion batteries: synthesis and performance enhancement methods†

Sourav Mallick, [a] Arjun Patel,[a] Xiao-Guang Sun, [b] Mariappan Parans Paranthaman, [b] Mingyao Mou,[a] Jethrine H. Mugumya, [a] Mo Jiang, [a] Michael L. Rasche,[a] Herman Lopez[c] and Ram B. Gupta *[a]

Received 21st October 2022
Accepted 17th January 2023

DOI: 10.1039/d2ta08251a

rsc.li/materials-a

Cost-effective production of low cobalt Li-ion battery (LIB) cathode materials is of great importance to the electric vehicle (EV) industry to achieve a zero-carbon economy. Among the various low cobalt cathodes, Ni-rich lithium nickel cobalt manganese oxide (NCM/NMC)-based layered materials are commonly used in EVs and are attracting more attention of the scientific community due to their high specific capacity and energy density. Various synthesis routes are already established to produce Ni-rich NCM cathodes with uniform particle size distribution and high tap density. Continuous production of highly pure Ni-rich cathode materials with uniformity in inter/intra-particle compositional distribution is critically required. On the other hand, cation mixing, particle cracking, and parasitic side reactions at higher voltage and temperature are some of the primary challenges of working with Ni-rich NCM cathodes. During the past five years, several advanced modification strategies such as coating, doping, core–shell, gradient structure and single crystal growth have been explored to improve the NCM cathode performance in terms of specific capacity, rate-capability and cycling stability. The scientific advancements in the field of Ni-rich NCM cathodes in terms of manufacturing processes, material challenges, modification techniques, and also the future research direction of LIB research are critically reviewed in this article.

[a]Department of Chemical and Life Science Engineering, Virginia Commonwealth University, Richmond, VA, 23219, USA. E-mail: rbgupta@vcu.edu

[b]Chemical Sciences Division, Oak Ridge National Laboratory, Oak Ridge, TN, 37831, USA

[c]Ionblox, Fremont, CA, 94538, USA

† Electronic supplementary information (ESI) available. See DOI: https://doi.org/10.1039/d2ta08251a

Dr Sourav Mallick is a post-doctoral scholar in the Department of Chemical and Life Science Engineering, Virginia Commonwealth University, USA. He received his PhD in 2021 from the Indian Institute of Technology, Kharagpur (IITKGP) in the field of Electrochemistry. He obtained his M.Sc. in 2015 from the IITKGP and his B.Sc. in 2013 from Presidency College, University of Calcutta, India in Chemistry. His research interests include functional materials for energy storage applications, including supercapacitors, and zinc–air, zinc-ion and Li-ion batteries. Currently, he is working in the field of slug-flow-derived NCM811-based cathodes for LIBs in the Gupta Research Lab at VCU.

Arjun Patel received his M. Tech degree in Chemical Engineering from the National Institute of Technology Warangal (NITW) in India. He has been pursuing his PhD degree in Chemical and Life Science Engineering at Virginia Commonwealth University (VCU) under the supervision of Prof. Ram B. Gupta since 2021. He is currently working on the development of layered cathode materials using a slug flow manufacturing process in the Gupta research Lab at VCU. His research interests include the optimization of processes in chemical engineering and the development of battery science for lithium-ion batteries.

1. Introduction

Affordable and clean energy for all is one of the primary goals to achieve sustainable development.[1] Undisrupted supply of clean energy is also critically required for industrial prosperity, which is directly related to economic growth. Although fossil fuels are widely used in various industrial sectors to produce energy, they affect the environment adversely by increasing the greenhouse gas (GHG) emission and hence they cannot be considered as a clean source of energy. According to the United Nation's Paris declaration, 23% of CO_2 emission is contributed by the transport sector and if the situation remains unchanged, the contribution will reach up to 50% by 2050. In order to control the CO_2 emission from transportation, the target is to power up 20% of vehicles with battery-electric, plug-in hybrid, and fuel cells by the year 2030.[2] Considering the global market, it is found that there is a 41% increment in EV registration within a one-year interval of 2019 to 2020.[3] Fig. 1a shows the reduction in life-cycle greenhouse gas emission with an increase in the electric vehicle registrations in 2021 and 2030 (predicted).[4,5] The increasing demand for EVs triggers the production of high performance and cost-effective Li-ion batteries (LIBs). It is worth mentioning that LIBs have already captured the global energy market since 1991 as the primary power source of laptop, mobile and other electronic devices due to their high useable capacity and energy density, long cycle life, light weight and eco-friendliness. Considering the increasing demand for LIBs in various sectors, the predicted growth of the LIB market within the next few years is shown in Fig. 1b.[6] As a result, the synthesis of efficient, cost-effective and robust LIB cathode materials is the need of this hour.

In 1990, Sony commercialized the $LiCoO_2$-based LIB, which was first used as the cathode by J. B. Goodenough's group in 1980.[7] Although the $LiCoO_2$-based LIB shows promising electrochemical performance, the major issue with this high cobalt-containing cathode material is the high battery fabrication cost. It is observed that the cost of cobalt is the highest among the various metals used for cathode preparation (Fig. 1c).[8] There is a steady increase in cobalt consumption per year due to battery production (Fig. 1d) and it also leads to the depletion of cobalt sources.[9] Moreover, the ethical as well as

Dr Xiao-Guang Sun is a senior scientist in the Chemical Sciences Division at Oak Ridge National Laboratory. He earned his PhD degree from Arizona State University. He has won two R&D 100 awards, authored and co-authored more than 100 journal publications with >6,150 citations and an "h-index" of 45. He has 26 inventions including 20 issued U.S. patents. He also won the ORNL Battelle's Distinguished Inventors in 2020. His present research focuses on development of novel salts, organic, polymeric, and composite electrolytes, as well as additives for different energy storage devices such as Li-ion, Mg-ion and Al-ion batteries.

Dr Parans Paranthaman is a corporate fellow at Oak Ridge National Laboratory. He is also fellows of the National Academy of Inventors, MRS, AAAS, APS, American Ceramic Society, ASM International and IOP. He earned his PhD from Indian Institute of Technology, Madras. He was a postdoctoral fellow with 2019 Chemistry Nobel prize winner Professor John Goodenough at the University of Texas, Austin. He joined Oak Ridge in May 1993. He has authored or co-authored more than 450 journal publications with >22,000 citations and an "h-index" of 73 and a total of >90 inventions including 57 issued U.S. patents related to his research.

Dr Mingyao Mou received her PhD degree in Chemical and Life Science Engineering from Virginia Commonwealth University in 2022. She received her M.S. degree in Pharmaceutical Analysis in 2018 from China Pharmaceutical University and a bachelor's degree in Pharmaceutics in 2015 from Chongqing Medical University. Dr Mou has been conducting research on experimental and process design, material synthesis and characterization in the field of pharmaceuticals and energy storage materials for 7 years.

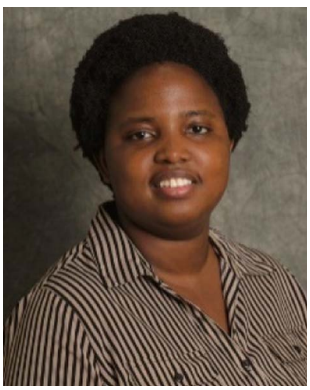

Jethrine H. Mugumya is currently a PhD student in the Chemical and Life Science Engineering program at Virginia Commonwealth University. She received her Bachelor's Degree in Chemical and Life Science Engineering from Virginia Commonwealth University in 2019. Her research is focused on optimizing the synthesis of lithium ion battery cathode materials.

political issues related to the excessive cobalt mining gravitate the EV industry to search for alternate LIB cathode materials with a less cobalt content. The U.S. Department of Energy has also taken a crucial step in this regard by setting a target to decrease the LIB production cost below \$60 kW h^{-1} by 2030, which is hard to achieve without reducing the cobalt content to 50 mg h^{-1} at the cell level.[8] As a result, remarkable progress in the field of low-cobalt/cobalt-less LIB cathode materials has been observed in the last few years and various active materials with layered (*i.e.* NCM and NCA), spinel (*i.e.* LMO and LNMO), olivine (*i.e.* LFP), disordered rock-salt type (with randomly distributed Li^+ and TM ions), *etc.*, structures have been already developed (Fig. 2a).[8,10,11] The electrochemical performances of the materials in terms of the voltage window, specific capacity and specific energy are well depicted by Muralidharan *et al.* in Fig. 2b.[8] The commercial success of cathode materials depends on various factors, including energy density, structural and chemical robustness during cycling, rate capability, synthesis method, product yield, availability, and production cost. Hence, all the materials are not applicable for practical usage. Among the above-mentioned materials, layered lithium nickel cobalt manganese oxide ($LiNi_xMn_yCo_{1-x-y}O_2$: NCM), specifically $LiNi_{1/3}Co_{1/3}Mn_{1/3}O_2$ (NCM111), is widely exploited for commercial LIB applications. Besides this, a $Li[Ni_{0.8}Co_{0.15}Al_{0.05}]O_2$ (NCA) cathode is used by Tesla Motors in Model S with a driving range of 270 miles per charge.[12] In order to decrease the manufacturing cost and to increase the energy density of NCM-based cathodes several NCMs with lower cobalt and higher nickel contents, such as NCM442, NCM532, NCM622 and NCM811, are also developed. It is observed that

Dr Mo Jiang is an assistant professor in the Department of Chemical and Life Science Engineering at Virginia Commonwealth University. Mo received a PhD in chemical engineering in 2015 from the Massachusetts Institute of Technology (MIT) and then became a postdoctoral associate there. He received a B.S. in biology in 2006 from Tsinghua University and an M.S. in chemical engineering in 2008 from the University of Illinois at Urbana-Champaign. Mo's main research interests include the advancement of scalable sustainable production of emerging materials with precise control for health and energy applications. Current projects include energy-efficient scalable manufacturing of essential (bio)pharmaceutical ingredients and active cathode materials for Li-ion batteries using a slug flow.

Dr Michael L. Rasche earned a B.S. in chemical engineering from the Rose-Hulman Institute of Technology and an M.S. and PhD in chemical engineering from the University of Illinois at Urbana-Champaign. He was a postdoctoral associate at the Massachusetts Institute of Technology. He currently serves as an assistant adjunct professor in the Department of Mathematics and Statistics at the University of North Carolina at Asheville and a research scientist at Virginia Commonwealth University. His research is in the development of mathematical models for the optimal design and control of crystallization operations.

Dr. Herman Lopez is a co-founder and CTO of Ionblox Inc. (former Zenlabs Energy) where he leads the development of their high-energy and high-power silicon-based lithium-ion batteries. He is a technical leader with over 20 years of experience developing advanced materials, processes and devices for the LIB, semiconductor, telecommunication and sensor industries. He has managed numerous government and customer programs working with industry, academia and National Laboratories. He previously served in multiple technical and management positions at Envia Systems, Intel Corporation and NeoPhotonics Corporation. Herman received his PhD in Materials Science from the University of Rochester, a B.S. in Chemistry from UCSD, and holds over 40 US issued patents.

Dr Ram B. Gupta is a Professor and the Associate Dean for Research and Graduate Affairs in the College of Engineering at Virginia Commonwealth University, Richmond, VA. He received a B.E. from the Indian Institute of Technology, an M.S. from the University of Calgary, and a PhD from the University of Texas at Austin, all in chemical engineering. He completed postdoctoral work at the University of California, Berkeley and the Management Development Program at Harvard University. Gupta served the U.S. National Science Foundation (NSF) as a director of the Energy for Sustainability program. For his academic excellence, he has been given many notable awards, endowed professorships, and 54 major research grants. According to Google Scholar his h-index is >60.

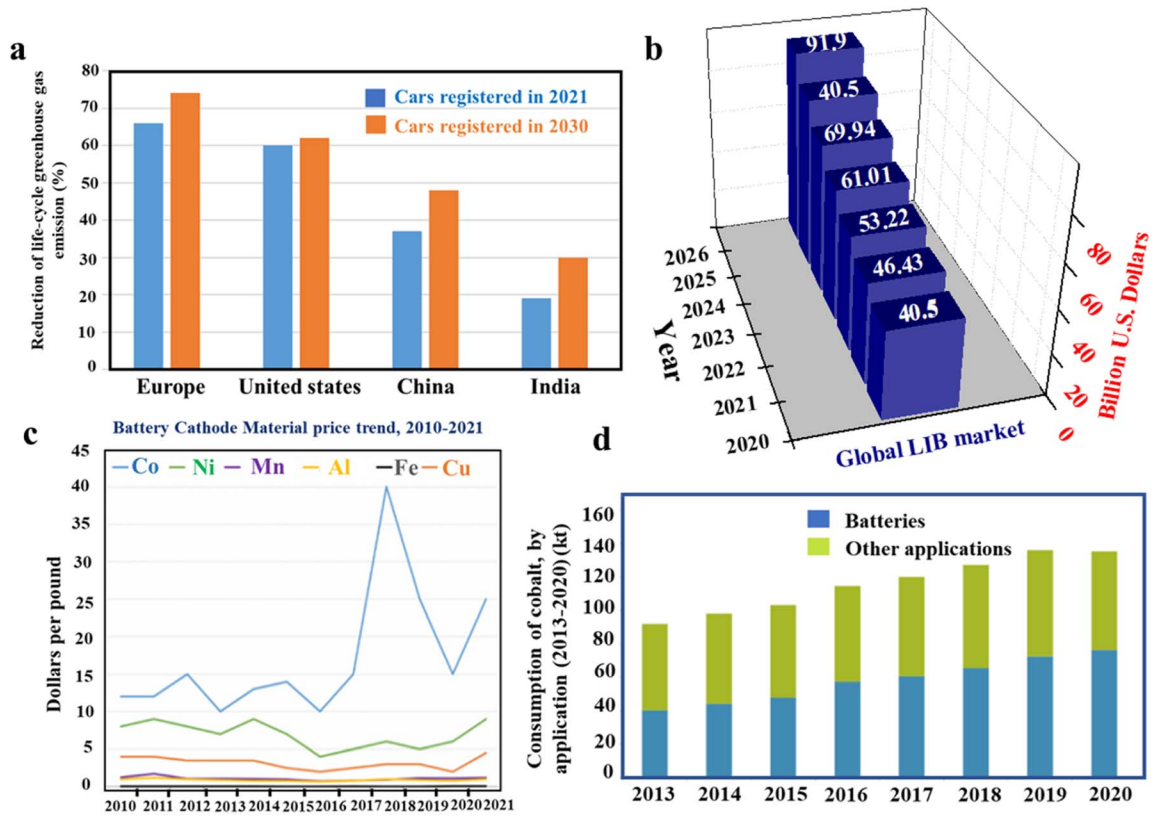

Fig. 1 Graphical representations of (a) reduction of life-cycle greenhouse gas emission with an increased number of registered EVs (data collected from ref. 4 and 5), (b) predicted growth of the LIB market within the next 4 years (data collected from ref. 6), (c) battery cathode material price trend, 2010–2021 (adapted with permission.[8] Copyright 2022, Wiley-VCH.) and (d) yearly consumption of cobalt (adapted with permission.[9] Cobalt institute, May 2021.).

the cost of the material steadily decreases with lowering the cobalt content (Fig. 2c), whereas the volumetric and gravimetric energy densities increase with increasing the nickel content in NCM-based cathode materials (Fig. 2d and e).[13] Various synthetic methods, including co-precipitation, solvothermal, spray dry, solid-state, *etc.*, are followed to obtain the materials.[14–17] The reaction conditions and selection of suitable reagents play a crucial role in achieving materials with a controlled particle size and regular morphology, which further determines the tap density as well as the charge storage performance of the active material.[18,19] In the case of the co-precipitation method the active material is generally obtained by a two step process, *i.e.*, precursor synthesis followed by lithiation, where the lithiation temperature plays a pivotal role in determining the tap density and electrochemical performance of the material. Although nickel-rich NCMs are advantageous in terms of low cost and high energy density, issues like cation mixing, side reactions and microcrack formation are the major hindrances in their commercial implementation.[20–22] Several modification techniques, including doping, surface coating, synthesis of core–shell, gradient synthesis, electrolyte additives, *etc.*, have been followed to date to mitigate these issues and provide low cobalt content active materials with commercial success.

This technical review provides a comprehensive overview of the synthesis and electrochemical performance of low cobalt content materials, specifically NCM-based LIB cathodes. The interrelation between the particle size, morphology, and tap density and their dependence on the synthesis conditions and reaction parameters are also critically analyzed in this article with the help of suitable examples. The development of a continuous synthetic platform to produce NCM-based battery materials in high yield, with high phase purity, and with improved control over the particle morphology and composition has high industrial importance. Our group has introduced a novel slug-flow-based continuous synthesis process for the production of NCM in the field of cathodes. The description of the slug-flow synthesis process together with the advantages over the already established synthesis methods will be covered in the review article. The advantages and disadvantages of the various strategies to further improve the electrochemical performance of Ni-rich NMC cathodes will also be discussed. The review article will give a broader perspective on the present status and the future research direction of low cobalt containing LIB cathode materials.

2. Various synthesis methods

The selection of an appropriate synthetic route for NCM-based cathode materials not only controls their morphology, particle size, and electrochemical performance but also determines the overall LIB fabrication cost. Hence, cost-effective synthesis of

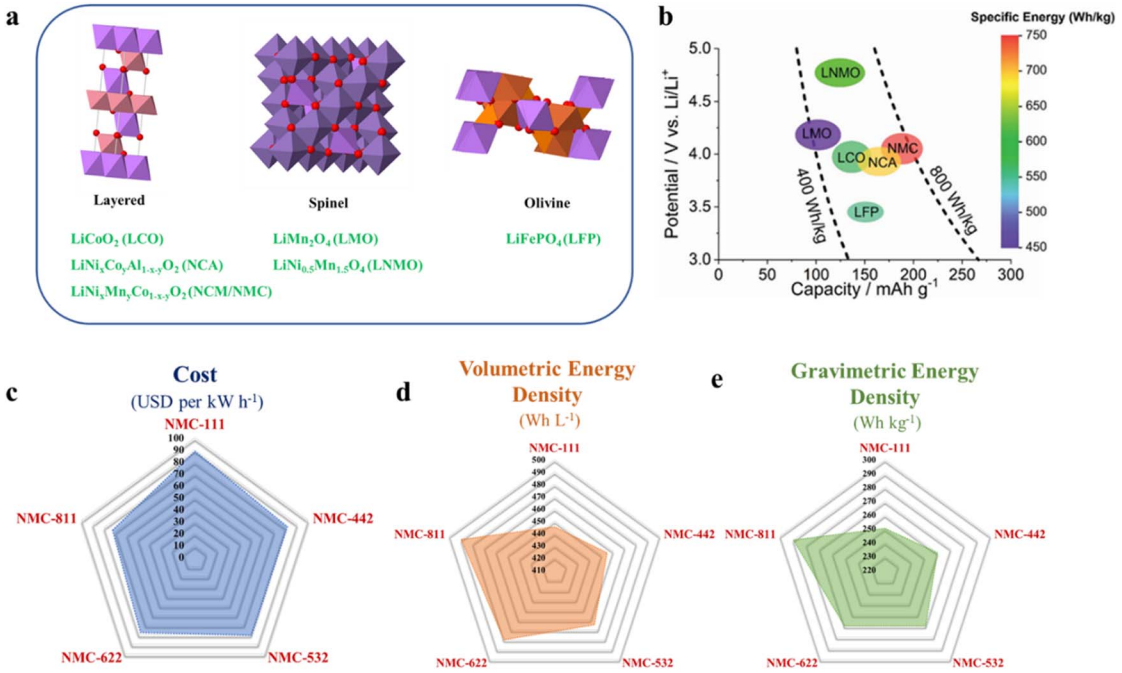

Fig. 2 (a) Crystal structures of various LIB cathodes, the structures are generated by using the ICSD database, and (b) electrochemical performance of LIB cathodes (adapted with permission.[8] Copyright 2022, Wiley-VCH.) and (c–e) graphical representation of change in the estimated cell material cost, and volumetric and gravimetric energy densities with decreasing Co-content in NCM-based cathodes (data collected from ref. 11 and 13).

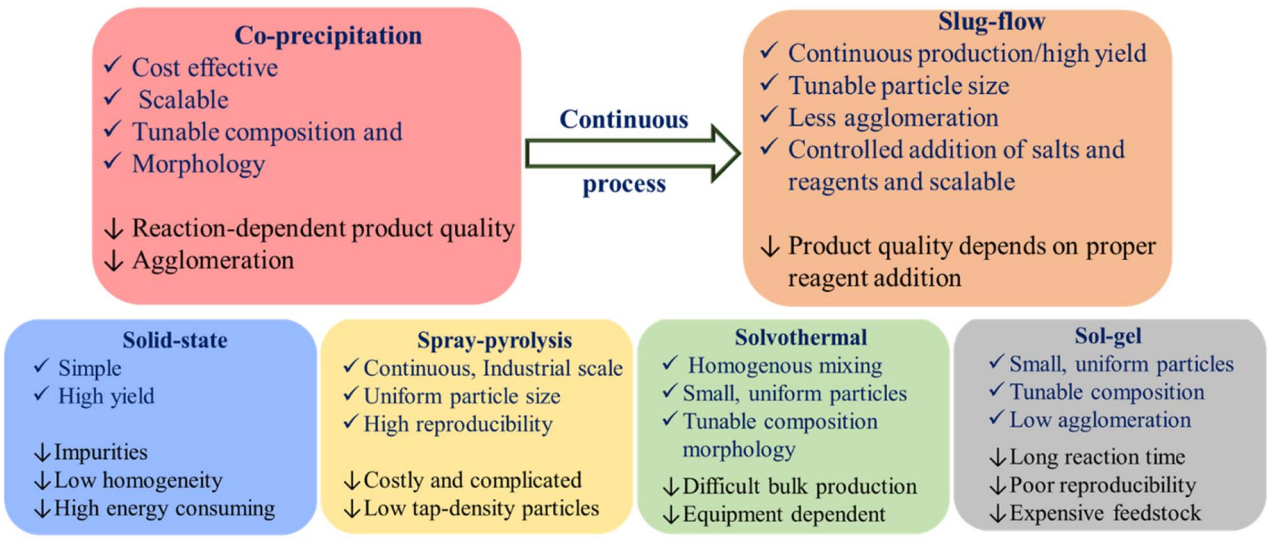

Fig. 3 Advantages and disadvantages of various synthesis processes of NCM based LIB-cathodes.

high-performance cathode materials in high yield for commercial LIBs is the need of this hour. Various routes, such as co-precipitation, solid-state, spray dry, solvothermal and sol–gel, are well explored to synthesize NCM cathodes. In an attempt to make the coprecipitation synthesis process continuous, our group has established a slug-flow reactor as a platform for battery cathode production. All of these techniques have their inherent advantages and disadvantages. Fig. 3 shows a comparative overview of all the synthetic procedures.

2.1 Co-precipitation

2.1.1. Precursor synthesis. Among various synthetic routes, co-precipitation is the most cost-effective and scalable method to produce NCM111 and low-cobalt NCM precursors in a high yield. The synthesis of NCM through co-precipitation involves two steps: synthesis of precursors followed by high temperature lithiation. It is worth mentioning that the nature of the precursor particle in terms of the yield, size distribution,

morphology and tap density are the important parameters to decide the electrochemical performance. The quality of the particles solely depends on the several reaction parameters, including pH, chelating agent concentration, temperature, stirring speed and metal salt concentration. Based on the anion involved in the precipitation of transition metal cations, co-precipitation processes are classified into three major categories: (i) hydroxide co-precipitation; (ii) carbonate co-precipitation; (iii) oxalate co-precipitation.[14] The flow chart (Fig. 4) describes the three co-precipitation routes with their advantages and disadvantages.

(i) Hydroxide co-precipitation. Although hydroxide co-precipitation is the most exploited synthetic strategy in the batch process, it mainly suffers from the oxidation of Mn^{2+} to higher oxidation states, leading to the formation of $NCM(OH)_2$ precursors with a substantial amount of impurities. The presence of impurities predominantly affects the electrochemical performance of the final lithiated oxide (NCM). Hence, maintaining an inert atmosphere throughout the synthesis is crucial to get impurity-free precursors. In the case of the hydroxide co-precipitation method, NH_4OH is used as the chelating agent and NaOH plays the role of a precipitant as well as pH- determining agent. Here, the metal ions first make a complex with NH_3 and then are slowly released to form the hydroxide according to the following reactions:[14]

$$M^{2+} + xNH_4OH\ (aq) \rightarrow M(NH_3)_n^{2+}\ (aq) + xH_2O \quad (1)$$

$$M(NH_3)_n^{2+}(aq) + yOH^- = M(OH)_2\ (s) + nNH_3 \quad (2)$$

The optimization of NH_4OH concentration and pH has a crucial effect on the hydroxide precursors' yield and the morphology. Our group has recently performed theoretical modeling on the effect of NH_4OH concentration and pH on the yield of NCM111 by the hydroxide co-precipitation method.[25] It was observed that the precursor synthesized at a pH of 11.8 and NH_4OH concentration of 0.1 M had the highest tap density. The modeling of the co-precipitation process relies on the solution of the mass action equations for the reversible reactions of all components in the aqueous phase, including dissociation of primary process inputs and formation of hydroxide and ammonia complexes with each of the transition metals. Combined with the solubility product equations for the transition metal precipitate (usually as hydroxide or oxalate), a saturation concentration for each transition metal is calculated for a set of reaction conditions (temperature, pH, ammonia concentration, *etc.*). The comparison of the initial and saturation concentrations of each transition metal can be used to calculate the yield and bulk composition of the precipitate at equilibrium. Additionally, for a dynamic simulation, time-dependent supersaturation can be used to determine nucleation, growth, and dissolution kinetics, which, together with aggregation and attrition rates, constitute the essential parts of the population balance equation that describes the evolution of the particle size distribution. Hydroxide co-precipitation is also proved to be beneficial for a number of low cobalt-NCM precursors with various compositions, such as $Ni_{0.6}Co_{0.05}Mn_{0.35}(OH)_2$, $Ni_{0.7}Co_{0.1}Mn_{0.2}(OH)_2$, $[Ni_{0.8}Co_{0.1-x}Fe_xMn_{0.1}](OH)_2$, $Ni_{0.21}Mn_{0.54}Co_{0.08}(OH)_2$, $[Ni_{0.95}Co_{0.025}Mn_{0.025}](OH)_2$,

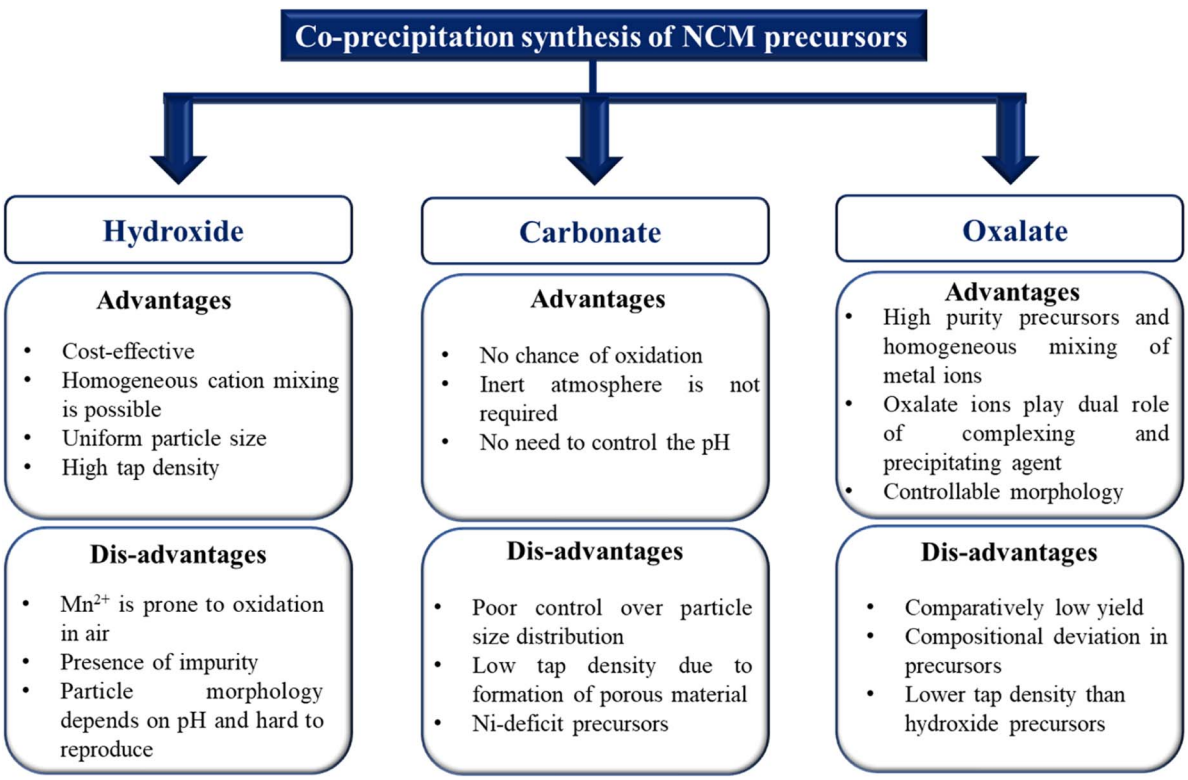

Fig. 4 Advantages and disadvantages of various co-precipitation methods to produce NCM precursors.

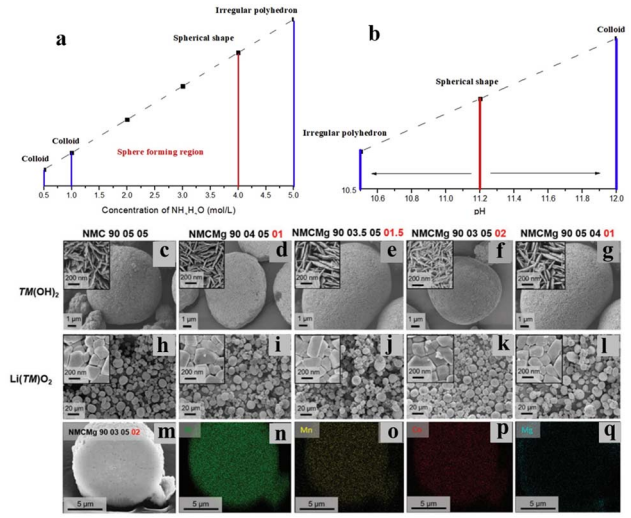

Fig. 5 (a and b) The effect of the concentration of $NH_3 \cdot H_2O$ and pH on the hydroxide precursor morphology (adapted with permission.[41] Copyright 2020, Elsevier.). (c–l) SEM images of hydroxide precursors ($TM(OH)_2$) and lithiated products ($LiTMO_2$) of NMC900505, NMCMg 90 040 501, NMCMg 9003.50501.5, NMCMg 90 030 502, and NMCMg 90 050 401. High-magnification SEM micrographs are shown in the inset of the corresponding (m–q) EDX elemental mappings of the NMCMg 90030502 powdered sample (adapted with permission.[28] Copyright 2022, Wiley-VCH.).

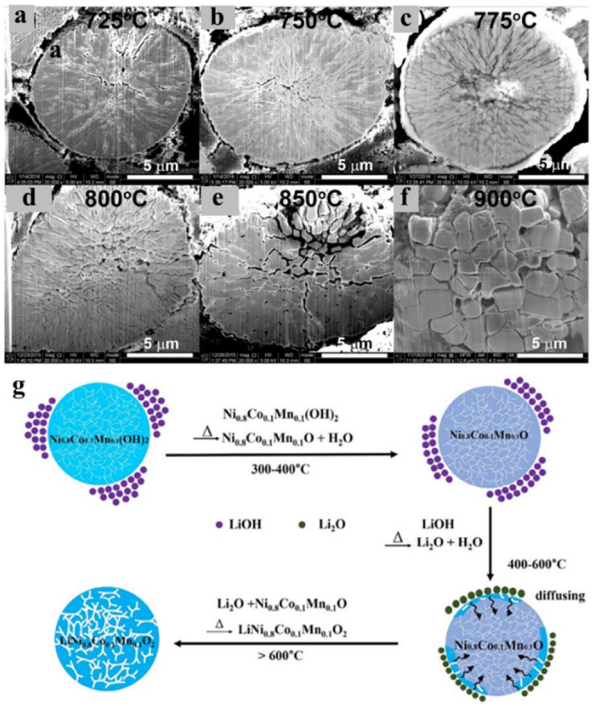

Fig. 6 (a–f) Cross-sectional SEM images of the $LiNi_{0.76}Mn_{0.14}Co_{0.10}O_2$ cathodes synthesised at different calcination temperatures after 200 cycles at C/3 within 2.7–4.5 V (adapted with permission.[34] Copyright 2018, Elsevier.). (g) Schematic illustration of the step-wise lithiation process of the hydroxide precursor (adapted with permission.[48] Copyright 2022, Elsevier).

$Ni_{0.8}Mn_{0.1}Co_{0.1}(OH)_2$, $Ni_{0.76}Mn_{0.14}Co_{0.10}(OH)_2$, $Ni_{0.90}Mn_{0.05-x}Co_{0.05}Mg_x(OH)_2$, *etc.*[26–41] However, obtaining and reproducing a specific morphology from the hydroxide co-precipitation method is challenging due to its dependency on the reaction parameters. Hence, rational control over the reaction parameters is critically required. Ding *et al.* have performed a detailed study on the growth of a NCM811-hydroxide precursor with a homogeneous particle size and uniform morphology by varying the $NH_3 \cdot H_2O$ and NaOH concentrations.[41] It was observed that as the $NH_3 \cdot H_2O$ concentration was increased from 0.5 to 4 mol L^{-1} the primary particles are packed more closely and the degree of sphericity increased (Fig. 5a). However, above 4 mol L^{-1} the metal ions bind with the ammonia strongly and decrease the crystal nuclei formation rate and agglomeration occurs. The pH of the solution controls the supersaturation limit by determining the solubility of the precipitate. According to their study, 11.2 is the optimum pH to achieve a spherical morphology, whereas lower and higher pH than that lead towards an irregular polyhedron and colloidal precipitate, respectively (Fig. 5b). A higher stirring speed also facilitates the growth of spherical particles by mitigating the issue of local supersaturation. They got the spherical hydroxide particles with uniform particle size distribution at a pH of 11.2 and $NH_3 \cdot H_2O$ concentration of 4 M L^{-1} at a stirring speed of 1000 rpm. Recently another group has synthesized coated NCM 811$(OH)_2$ particles using 4 M NH_4OH and NaOH at a pH of 11.7.[37] The core is composed of Ni : Mn : Co = 8 : 1 : 1 and the surface is made of Mn : Co = 1 : 1, which provides structural robustness during cycling. Lithiation was done at 775 °C for 50 h. It is also observed that the optimum co-precipitation reaction conditions will also vary with varying metal salts, in terms of the counter anion, concentration, composition and reaction process. As an example, Yoon *et al.* have synthesized spherical $[Ni_{0.95}Co_{0.025}Mn_{0.025}](OH)_2$ precursors in a batch process using sulfate salts of three transition metals and NaOH (4 M) as the precipitating agent and NH_4OH (molar ratio of NH_4OH to transition metal = 1.2) as the chelating agent.[39] The as-synthesized dried hydroxide precursor was crushed with $LiOH \cdot H_2O$ (Li: (Ni + Co + Mn) = 1.01 : 1 molar ratio) and calcined at 700 °C for 10 h to obtain hierarchically shaped $Li[Ni_{0.95}Co_{0.025}Mn_{0.025}]O_2$ with a uniform secondary particle size of 10 μm. The LIB fabricated using the material achieves a specific capacity of 238 mA h g^{-1} at 0.1C within the voltage window of 2.7–4.3 V *vs.* Li/Li^+. The replacement of Co with another metal, such as Fe^{3+}, Mg^{2+}, *etc.* in a Ni-rich NCM structure is found to be beneficial, as it mitigates the issue of cation mixing and reduce the overall cost of the cathode material.[28,31] Cation-substituted spherical NCM can be synthesized through the hydroxide co-precipitation method by only introducing an additional metal salt in the exact molar ratio and maintaining appropriate reaction conditions. Martin *et al.* have shown that, with the increase of the Mg^{2+} content up to 2 mol% the density of the NCM hydroxide particles is increased (Fig. 5c–g). It was also observed that the 50–200 nm granular primary particles are agglomerated to form bigger granular secondary particles (Fig. 5h–l). From EDX analysis it was found that the secondary particles have low porosity and uniform distribution of Ni, Co, Mn and Mg (Fig. 5m–q).[28]

(ii) Carbonate co-precipitation. The major advantage of the carbonate co-precipitation method is that it is free from oxidation related issues and hence an inert atmosphere is not required. The quality of the carbonate precursors does not depend on the pH. The carbonate coprecipitation method is already explored in the synthesis of NCM111, various low cobalt and cobalt-free NCM precursors.[42–45] In this case, Na_2CO_3 is generally used as the precipitating agent and NH_4OH plays the role of a chelating agent. The following reactions are involved:

$$M^{2+} + xNH_4OH\ (aq) \rightarrow M(NH_3)_n^{2+}\ (aq) + xH_2O \quad (3)$$

$$M(NH_3)_n^{2+}(aq) + yCO_3^{2-} = MCO_3\ (s) + nNH_3 \quad (4)$$

Materials with a random morphology and low tap density are the major drawbacks for the carbonate coprecipitation method. Also, there is a high possibility of cation deficit product formation in the case of high Ni-containing NCM carbonate precursors.

(iii) Oxalate co-precipitation. Oxalate co-precipitation is advantageous in terms of uniformity in the particle size and homogeneity in the morphology. Oxalate plays a bi-functional role of a chelating as well as precipitating agent. NH_4OH plays the crucial role in maintaining pH > 8.0, which is required to form micrometer-sized secondary particles. Generally, $(NH_4)_2C_2O_4$ or $H_2C_2O_4$ is used as the oxalate ion source and forms precipitates through the following chemical reactions:

$$M^{2+} + xNH_4OH\ (aq) \rightarrow M(NH_3)_n^{2+}\ (aq) + xH_2O \quad (5)$$

$$M(NH_3)_n^{2+}(aq) + yC_2O_4^{2-} = MC_2O_4\ (s) + nNH_3 \quad (6)$$

Although this process is used for synthesizing various low cobalt NCM precursors, such as NCM622, NCM811, *etc.*,[46,47] the lower water solubility of oxalate salts reduces the yield of the product. Moreover, the tap density of the as-synthesized NCM-oxalates is found to be less than that of the corresponding hydroxides. However, the oxalate co-precipitation method is still regarded as the favorable and consistent process to obtain NCMs with a defined morphology.

2.1.2. Lithiation of the precursors. The precursors, synthesized by various co-precipitation methods, must be lithiated to obtain the final active cathode material. The dried precursors are first mixed and crushed with suitable Li salts, such as LiOH, $LiCO_3$, *etc.*, followed by high temperature calcination. Hence, the particle size of the final material largely depends on the heating rate, heating steps, the highest calcination temperature and the duration of calcination. Although a high temperature is required for complete diffusion of Li^+ into NCM and high crystallinity, it often causes the agglomeration of the particles and a greater extent of cation mixing. As a result,

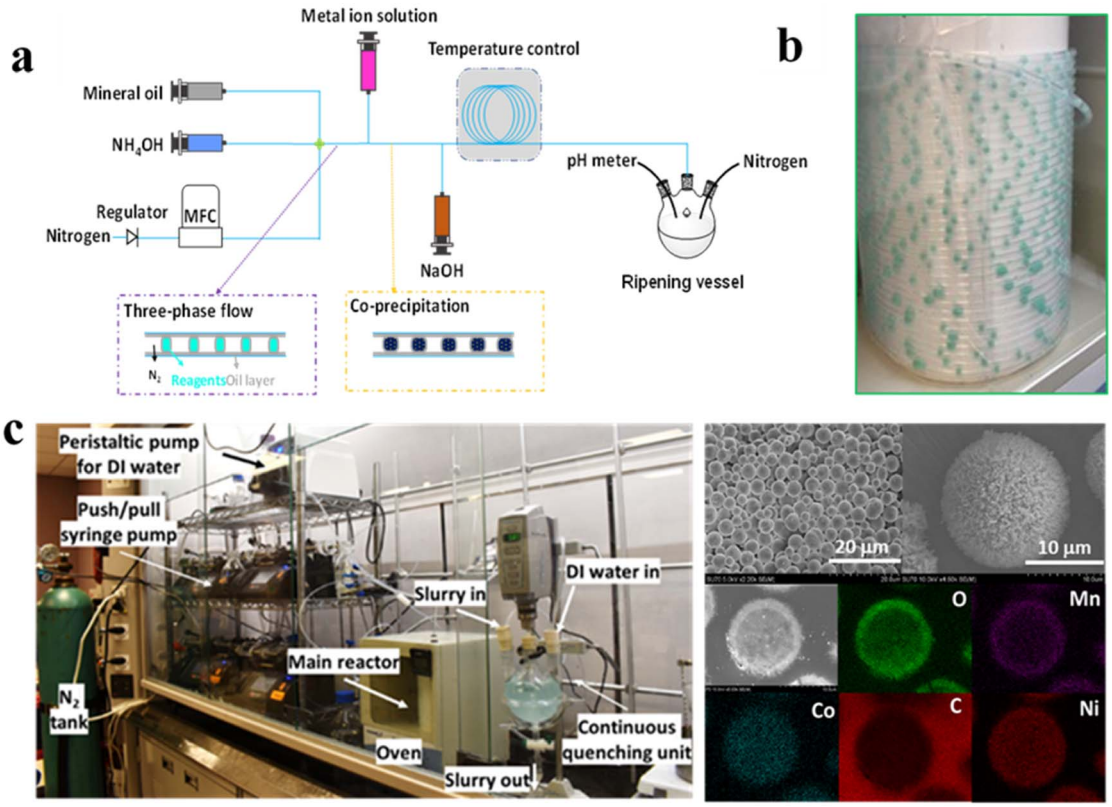

Fig. 7 (a) Schematic illustration of a three phase slug-flow manufacturing setup for NCM811 hydroxide production (adapted from ref. 23); (b) digital photograph of slugs formed inside the tubular reactor, and (c) digital photograph of the slug-flow manufacturing platform and the SEM images of slug-flow-derived NCM811 oxalate precursors with a uniform morphology and size distribution (adapted from ref. 24).

retaining the morphology of the precursor particles becomes a challenging task. Hence, an appropriate tradeoff between the highest temperature and sintering time is critically required to retain the particle size and morphology. Zheng *et al.* have performed a systematic study on the effect of calcination temperature on the morphology and the extent of cation mixing in $LiNi_{0.76}Mn_{0.14}Co_{0.10}O_2$ and published their observation in 2018.[34] Here, co-precipitation reaction derived spherical $Ni_{0.76}Mn_{0.14}Co_{0.10}(OH)_2$ was mixed with LiOH and subjected for pre-calcination at 500 °C for 10 h followed by high temperature calcination from 725 to 900 °C for 20 h in the ambient air atmosphere at a heating rate of 3 °C min^{-1}. It was observed that, initially the extent of Li/Ni cation mixing decreased within the temperature rage of 725 °C to 775 °C and then started to increase up to 900 °C. At the temperature of 775 °C the mixing was found to be minimum with the highest ($I_{(003)}/I_{(104)}$) of 1.33, signifying the fine layered structure of Ni-rich NCM. From the SEM images, it was found that although the spherical morphology was retained at all the calcination temperatures, deformation in the primary particle shape and the presence of grain boundaries were observed >850 °C, resulting in enlarged voids in secondary particles. As a result, the electrochemical performance of Ni-rich NCM deteriorates in terms of specific capacity and cycling stability with increasing the calcination temperature due to the increased extent of micro-crack formation (Fig. 6a–f) upon potential induced Li^+ ion intercalation/de-intercalation.[34] Recently, Tang *et al.* have reported a similar kind of study, but within a wider range of temperature from 300 to 1080 °C for NCM811.[48] From morphological observations at different temperature, it was observed that at 300 °C, LiOH blocks were attached on the spherical particles of $Ni_{0.8}Mn_{0.1}Co_{0.1}(OH)_2$ and as the temperature increases LiOH decomposes and uniformly diffuses into the NCM moiety keeping the morphology unaltered (Fig. 6g).[48] It can be clearly seen that the change in the particle size in the recrystallization process is closely related to temperature. Therefore, proper optimization of the calcination time, heating rate and highest temperature is key to achieving a good particle morphology and electrochemical performance. The use of comparatively lower calcination temperature for a longer time with a slow heating rate may be fruitful to retain the precursor morphology.

2.1.3 Continuous co-precipitation synthesis through a slug-flow reactor. The conventional co-precipitation manufacturing is mainly based on stirred tanks in batch mode (and recently in continuous mode), with temperature, pH, and stirring utilized to control the product quality. Batch-mode stirred tank reactors also suffer from intrinsic batch-to-batch variability and difficulty in scale-up, can cause particle breakage due to high shear, and require high energy/time.[49–52] The issues become much worse for particles with complex structures. Recently continuous-mode stirred tanks were shown to improve particle uniformity, although the problem is not entirely solved. Similar challenges and fundamental problems exist for pharmaceutical particles produced with stirred tanks. Recently the slug-flow process is proved to be useful in rapidly generating uniform crystals of various organic molecules[53,54] and inorganic molecules.[55] Hence, we have adapted the process for synthesizing NCM-precursor particles in high yield (Fig. 7a).[23] Liquid and gas are introduced into one end of the tube at selected flow rates to spontaneously generate alternating slugs of liquid and gas that remain stable while crystallization occurs in each liquid slug. Mixing within each stable self-circulating slug (Fig. 7b) is tuned by using the slug aspect ratio through specification of liquid and gas flow rates. The milli-fluidic reactor and the flow conditions are rationally monitored in order to form hydrodynamically stable slugs.[56] In addition, selective injection of additional reactants in individual slugs is also possible to carry out the follow-on reactions. The slug-flow reactor offers spatially uniform reaction conditions (kinetics and hydrodynamics) for each particle throughout the nucleation-growth process, leading to the formation of uniform particles with controlled composition and properties (Fig. 7c).[24] Uniform-sized NCM precursors with wide variation in composition, including high cobalt (NCM111) to cobalt free (NCM901), are successfully produced using a three-phase slug-flow reactor.[24] The production rate and scale can be tuned without changing the equipment as with any co-precipitation process, slug-flow synthesis of precursors (*e.g.*, oxalates and hydroxides). The reactor also has a high prospect of producing Ni-rich NCM precursors with core–shell or concentration gradient structures.

2.2 Solid-state synthesis

Solid-state synthesis is one of the most commercially used methods to synthesize NCM-based cathodes, specifically NCM111.[57] Easy handling and less-complicacy in the preparation of reaction mixtures are the two primary advantages of this synthetic procedure. This involves the grinding of metal salt precursors, followed by high temperature calcination (<800 °C) in the presence of oxygen. Unlike co-precipitation, in this case, there is no need to maintain the reaction environment in terms of pH, chelating agent concentration, *etc.* Hence it is widely used in commercial-scale production of NCM. However, proper grinding and homogeneous mixing of the salts are critically required to achieve NCM with exact stoichiometry. The nature of the product also depends on the duration of hold time at high temperatures. With an increased duration of the hold time the metal ions get a longer time to diffuse towards the suitable crystal sites, resulting in a stable structure with a defined morphology. High energy consumption and the presence of impurities are the major drawbacks of this method. It is observed that there are very few reports on the solid-state synthesis of low-cobalt NCMs. The lack of homogeneity during mechanical mixing limits the extensive application of the solid-state method in the synthesis of low-cobalt NCMs.[58,59] In order to get rid of inhomogeneity related issues, Shi *et al.* dissolved metal acetate salts and $LiNO_3$ in ethanol and stirred well, afterward the mixture was subjected to combustion at 500 °C and then the combustion product was ground well.[59] Finally, the product was subjected to calcination at three different temperatures, *i.e.* 700, 800 and 900 °C, to obtain three different $[Li_{0.2}Mn_{0.54}Ni_{0.13}Co_{0.13}]O_2$ and they are abbreviated as LMNCO-700, 800 and 900, respectively. Among these materials, LMNCO-800 showed

good rate capability with the specific capacities of 238.6 and 165.0 mA h g^{-1} at current densities of 200 and 2000 mA g^{-1}, respectively.

2.3 Sol–gel synthesis

The primary step in the sol–gel method is to make a homogeneous solution of the reactants, followed by gelation of the mixture by using a suitable complexing agent. Then the gel is heated and dried to form zero-gel and subjected to high-temperature calcination to get the final product. Small and uniform particle size distribution, tunable compositional variation, and less agglomeration are the major advantages of this method. Some research groups utilized this method to synthesize various low cobalt NCMs, such as $LiNi_{0.9}Co_{0.05}Mn_{0.025}Mg_{0.025}O_2$, $LiNi_{0.8}Co_{0.1}Mn_{0.1}O_2$, *etc.*[60,61] In the year 2013, Lu *et al.* have reported that $LiNi_{0.8}Co_{0.1}Mn_{0.1}O_2$ derived from the sol–gel method shows lower Li^+/Ni^{2+} mixing, less particle aggregation and a greater BET surface area compared to co-precipitation derived NCM.[61] Later in another study the same process was utilized to synthesize $LiNi_{0.9}Co_{0.05}Mn_{0.025}Mg_{0.025}O_2$.[60] In both cases, citric acid is used as the complexing agent. As the Li salt is generally added at the beginning of the reaction, homogeneous mixing of Li with other metal salts was possible in this case. A longer reaction time, poor reproducibility, and expensive raw materials make the sol–gel process less suitable for commercial production.

2.4 Solvothermal synthesis

The solvothermal technique is a well-known approach to synthesize nanomaterials with a defined morphology, uniform particle size distribution and composition. In this process, the reaction mixture is put into a Teflon-lined stainless-steel autoclave and then the autoclave is placed inside an oven at about 150–200 °C, specifically when water is the solvent. Inside the autoclave, the chemical reaction takes place under constant temperature and high pressure, which facilitates the formation of well-defined and highly crystalline precursor particles. Similar to the co-precipitation process, the final lithiated oxide material is achieved by mixing the precursor with a lithium salt, followed by high-temperature calcination in an oxygen atmosphere. There are few reports on the solvo/hydrothermal synthesis of low cobalt NCM precursors.[62–66] It is interesting to notice that most of the as-synthesized NCM precursors have a well-defined morphology and the lithiated materials show good electrochemical performance. Fig. 8a–e show that the morphology of the solvothermal product crucially depends on the reaction time.[66] The yield of the solvothermal product also largely depends on the capacity of the autoclave and bulk production is hard to achieve. The equipment dependency limits its commercial application.

2.5 Spray pyrolysis synthesis

Spray pyrolysis is a well-exploited continuous synthesis technique to produce transition metal oxides on an industrial scale. This technique is also utilized to synthesize NCM-based battery cathodes. The synthesis of NCM through spray pyrolysis primarily involves two steps: (i) nebulizer-assisted formation of micro-sized droplets of transition metal and lithium salt solution and (ii)

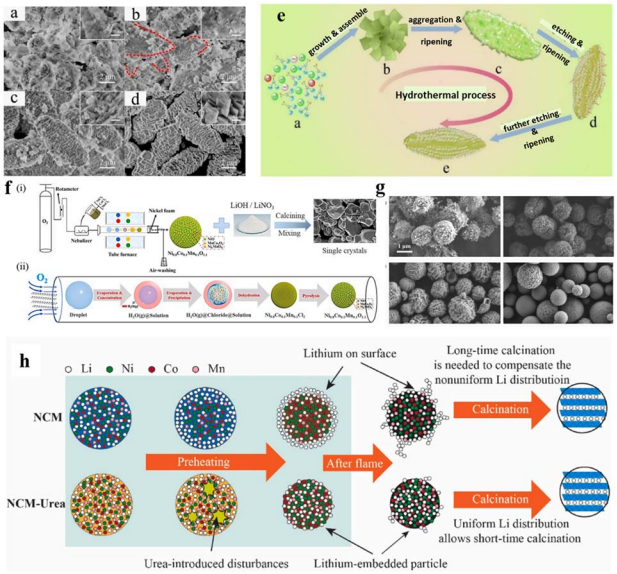

Fig. 8 FESEM images of $Ni_{0.8}Co_{0.1}Mn_{0.1}CO_3$ precursors obtained at different hydrothermal reaction times: (a) 1 h, (b) 2 h, (c) 4 h, and (d) 8 h and (e) schematic illustration of the growth of an olive-like crystal structure (adapted with permission.[66] Copyright 2019, Wiley-VCH.). (f) Schematic illustration and formation mechanism of the $Ni_{0.8}Co_{0.1}Mn_{0.1}O_{1.1}$ microsphere synthesized by spray pyrolysis from chloride solution (adapted with permission.[68] Copyright 2020, Elsevier), (g) SEM images of the as-synthesized samples: NCM and NCM-urea with lithium nitrate (both precursor and lithiated materials) and (h) the proposed mechanism for the difference between NCM and NCM-urea routes (adapted with permission.[69] Copyright 2022, Elsevier.).

placing the micro-droplets inside a high temperature reactor, where the uniform particles of NCM are produced as an outcome of consecutive chemical reactions inside the micro-droplets. Phase pure materials with uniform particle size distribution can be produced with high yield and reproducibility through this technique.[67] The particle size and the morphology of the synthesized materials exclusively depend on the size of the nebulizer, residence time, reactor temperature, precursor concentration, *etc.* A few of the research groups get success in producing NCM811 with uniform morphological distribution and small particle size.[68–71] Zhu *et al.* have synthesized sub-micron single crystal NCM811 using the spray pyrolysis technique (Fig. 8f).[68] An aqueous solution of $NiCl_2 \cdot 6H_2O$, $CoCl_2 \cdot 6H_2O$, and $MnCl_2 \cdot 4H_2O$ (8 : 1 : 1) was aerosolized using an ultrasonic nebulizer at a frequency of 1.75 MHz and carried into a tube furnace (800 °C) at a constant 3 L min^{-1} by an oxygen flow. The precursor powder was collected using Ni-foam and the residual chlorine and H_2O were evaporated by heat treatment at 400 °C for 3 h to obtain hybrid oxides NiO–$MnCo_2O_4$–Ni_6MnO_8 (molecular formula: $Ni_{0.8}Co_{0.1}Mn_{0.1}O_{1.1}$). Subsequently, the as-prepared precursor was mixed with a lithium salt (LiOH or $LiNO_3$) and calcined at 800 °C to obtain NCM811. This is an efficient strategy for the industrial synthesis of single-crystal cathode materials using flux addition and repeated sintering. Single-crystal NCM811 with submicron particle size is beneficial in terms of better structural stability by

preventing the generation of intergranular cracks. Recently, another group has reported an accelerated synthesis of NCM811 in the presence of urea as the additive through flame-assisted spray pyrolysis (Fig. 8g and h).[69] It was observed that the precursor solution with 2.5 wt% urea shows a shortened calcination time of only 20 min. Without any preheating and temperature ramping stages to obtain a perfect layered structure. The low tap density of the as-synthesized materials and hence lower volumetric capacity are the major drawbacks of this technology. Moreover, the technology is costly and also complex.

3 Correlation between the synthesis method, particle properties and electrochemical performance

The electrochemical performance of the battery largely depends on the nature of the cathode particles, more precisely on the parameters like size, particle size distribution (PSD), porosity, morphology, *etc.* (Fig. 9). Those parameters have a direct effect on the tap density of the material. The material with a higher

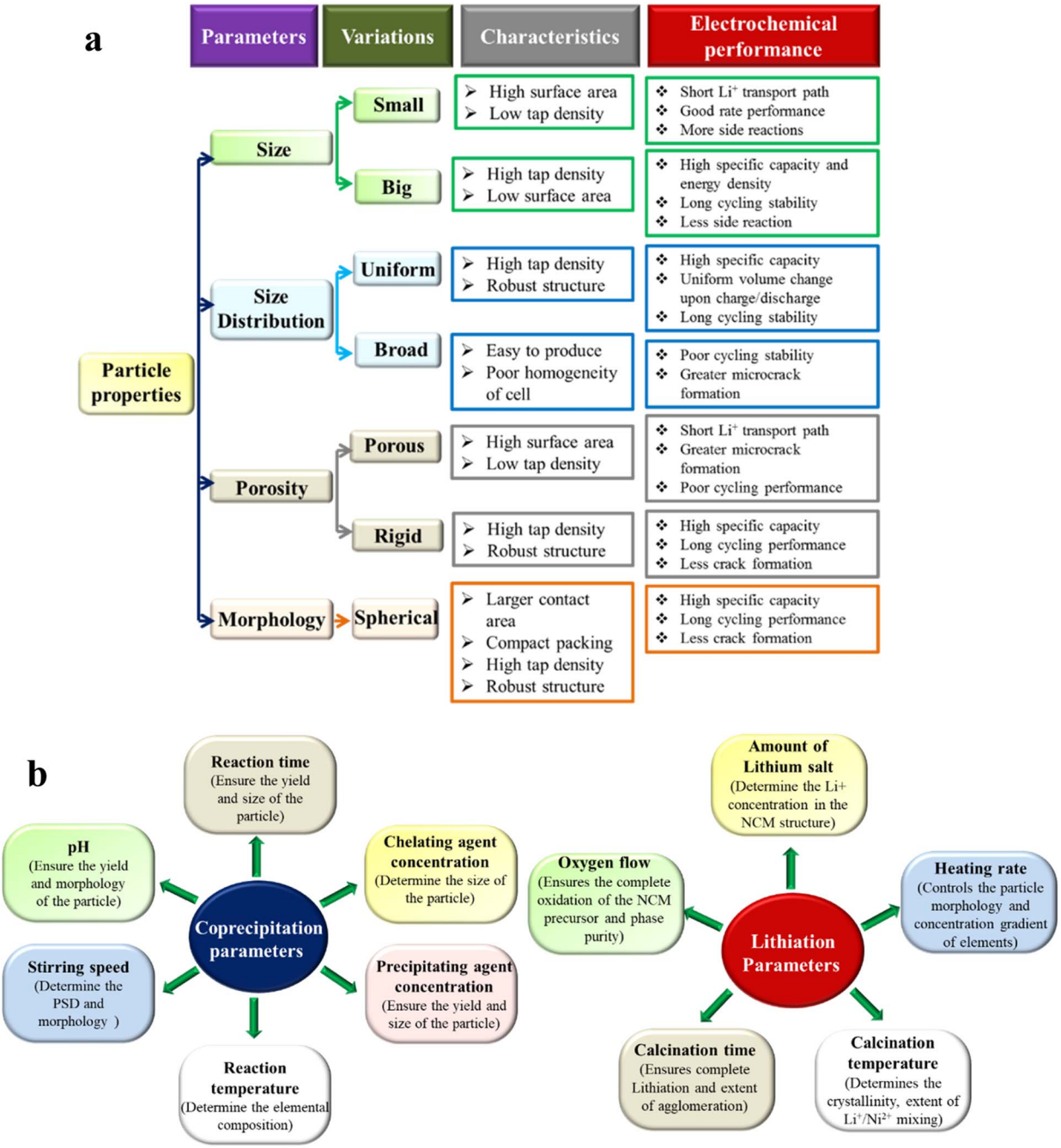

Fig. 9 Correlation between the (a) particle properties with the electrochemical performance and (b) effect of co-precipitation and lithiation parameters on particle properties.

tap density is beneficial to achieve high volumetric capacity and energy density. Materials with big (optimum size of ~10–20 μm) and non-porous rigid secondary particles generally offers higher tap density. It is true that the small and porous particles possess a short Li^+ transport path and show good rate capability. However, the poor volumetric energy density hinders their commercial application in high energy applications, like EV technology. On the other hand, the cycling performance of the cathode is determined by the PSD and the porosity of the polycrystalline NCMs. The uniformly distributed particles show similar volume shrinkage upon delithiation at a certain voltage and achieves greater structural robustness. Materials with highly porous particles possess a larger active surface area and electrolyte can penetrate deep into the bulk, which aggravated the extent of side reactions and promote microcrack formation. It is already discussed that the microcrack formation and collapse of secondary particles are the primary reasons behind the poor cycling performance. Among the various morphologies the big spherical particles show good packing density, structural robustness and high tap density and hence widely explored for high energy and long-term applications. The single crystal morphology is also promising to achieve crack-free longer cycling stability of Ni-rich NCM-based cathodes, which is discussed in a later part of the review.

From the above discussion it can be concluded that big (10–20 μm scale), uniform, spherical and rigid Ni-rich NCM particles are ideal for high energy and long-term applications. It is worth mentioning that the NCM particle properties are primarily determined by the nature of the NCM precursor. The properties of NCM precursors solely depend on the synthetic method followed to produce them. Among the various well-established synthesis procedures, the co-precipitation method is the most efficient one to produce NCM precursors with a controlled size, morphology and composition. However, the co-precipitation product nature is dependent on the parameters like pH, NH_4OH concentration, stirring speed, reaction temperature, precipitating agent concentration, *etc.* The reaction temperature and time have an important effect on the elemental composition of the product. The composition varies based on the precipitation reaction kinetics of the various transition metals. Moreover, the final lithiated NCM-oxide is obtained by calcination of the precursor at high temperature in an oxygen flow. In this step, the important parameters are the amount of lithium salt, calcination temperature, heating rate, calcination time, oxygen flow, *etc.* The effect of those parameters is described in Fig. 9. The continuous production of phase pure, high tap density, spherical NCM particles is one of the future aspects of battery research. We have tried to establish a three-phase slug-flow manufacturing platform to make the co-precipitation process continuous and produce NCMs is bulk amounts. The flow rate, viscosity of the liquids, size of the slugs, tube diameter and length, salt concentration, efficient reagent addition, internal mixing, *etc.,* are a few of the important parameters that determine the product quality in this case.

4 Challenges of low cobalt NCM materials

4.1 Cation mixing

Cation mixing, more precisely Ni/Li mixing, is a standing issue for high Ni-content NCMs, as it adversely affects the Li^+ diffusion kinetics throughout the material and deteriorates the cycling, rate performance, and thermal stability of LIBs. The phenomenon was first observed in a $LiNiO_2$-based cathode.[72] The extent of cation mixing in the bulk phase is commonly analyzed by using the ratio of the peak intensity of (0 0 3)/(1 0 4). The migration of Ni^{2+} results in the phase change of the NCM material from layered to spinel and rock-salt phases and hinders the facile diffusion of Li^+ throughout the material (Fig. 10a). The reason behind the cation disorder can be described through the following three points: (i) size effect, (ii) magnetic interaction and (iii) kinetic effect.

4.1.1 Similarity in size. The similarity in the radius of Ni^{2+} (0.69 Å) and Li^+ (0.76 Å) is considered as one of the driving forces behind Ni/Li mixing in the layered structure of NCM. The phenomenon primarily takes place during a long-term charge–discharge process. More precisely, during the charging of the battery, the Li^+ ions slowly de-inserted from the cathode and Ni^{2+} occupied the vacant sites. Although the Li^+ ions try to re-insert into their initial sites during the discharge step, their easy insertion is hindered by the pre-occupied Ni^{2+} ions, leading to an irreversible capacity loss in each cycle.[73] In this context, it is worth mentioning that the cation mixing is generally observed in high Ni-content layered NCMs, where the population of Ni^{3+} is much higher than that of Ni^{2+}. It indicates that the size is not the only governing factor behind the cation mixing.[74]

4.1.2 Superexchange interaction. The crystal field splitting of d-orbitals of transition metals (TMs), which are present in the NCM moiety (*i.e.* $Ni^{2+/3+}$, Mn^{4+} and Co^{4+}), into e_g and t_{2g} and the resulting superexchange phenomenon with neighboring TMs through the bridged oxygen anion are the primary reasons behind the cation mixing in high-Ni NCM cathodes. It is observed from the crystal field splitting profiles (Fig. 10b) that all of the above-mentioned transition metal ions, except Co^{4+}, have unpaired electrons either in t_{2g} or e_g.[75] Due to the presence of unpaired electrons in TM ions, they form intra-plane (90°) or interplane (180°) superexchange interactions with the neighboring TMs through bridging O^{2-} (Fig. 10c).[75] According to the Goodenough–Kanamori–Anderson rule,[76,77] due to the formation of stronger sigma bonds the linear interplane interaction is stronger than the former one and this concept can be used to rationalize the Ni/Li mixing phenomenon. As the 180° Ni^{2+}–O–Ni^{2+} interaction is stronger than the 90° Ni^{2+}–O–Ni^{2+} interaction, the Ni^- ions ($Ni^{2+/3+}$) occupy the Li^+ sites to form a strong interplanar superexchange interaction and stabilize the structure.[75,77] In the case of high Ni-content NCMs, where the Ni is present in a mixed-valence state of +2 and +3, Ni^{3+} first occupies the Li^+ positions and then transformed into Ni^{2+} with spin-flip and stabilize the

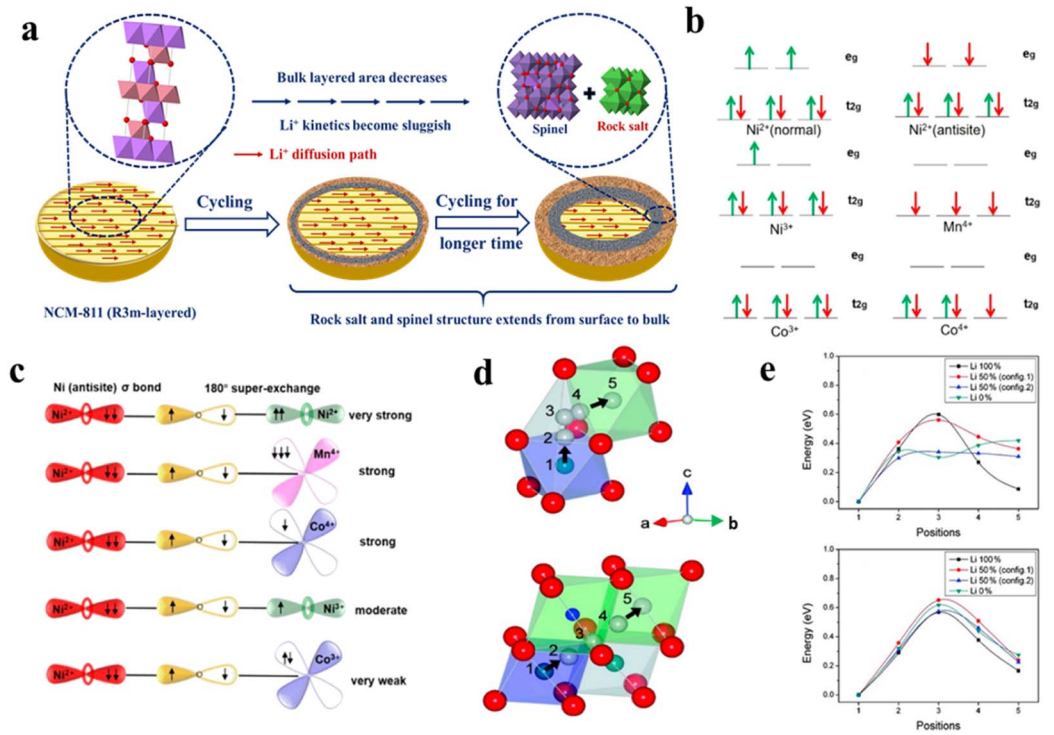

Fig. 10 (a) Schematic illustration of phase change of the NCM811 cathode upon cycling. (b) Electronic configurations for transition metal ions in NCM and (c) schematic for 180° superexchange interaction (adapted with permission.[75] Copyright 2017, American Chemical Society). (d) The $O_h \rightarrow T_d \rightarrow O_h$ and $O_h \rightarrow V_O$ site $\rightarrow O_h$ routes of Ni–Li migration and (e) the corresponding energy barriers (adapted with permission.[80] Copyright 2011, American Chemical Society.).

system by a strong super-exchange interaction.[78,79] The exchange between magnetic Ni^{2+} and non-magnetic Li^+ stabilizes the NCM crystal lattice by antiferromagnetic interaction. It is also observed that the presence of non-magnetic Co^{3+}, having zero unpaired electrons, can also relieve the magnetic frustration and mitigate the Ni^{2+}/Li^+ mixing to a large extent. On the other hand, the extent of Ni^{2+}/Li^+ mixing increases with the increase of magnetic Mn^{4+} in the NCM structure. Hence, it can also be claimed that the inherent magnetic frustration is one of the reasons behind the Ni/Li mixing in NCM crystals and the highest and lowest degrees of cation mixing are observed in NCM811 and NCM111, respectively.

4.1.3 Low migration energy barrier. The Ni/Li mixing is further facilitated by the low migration energy barrier of Ni^{2+} in the NCM moiety. From *ab initio* calculations, it is found that in the case of $Li(Ni_{1-x}Co_x)O_2$, the Ni^{2+} migration energy barrier through the Oh–Td–Oh path (Fig. 10d) is comparable to the Li-ion migration barriers in NCM materials (Fig. 10e).[80] Moreover, long term charge–discharge cycling or high temperature experiments create oxygen vacancies (V_O) inside the NCM crystal structure and this further promotes the Ni^{2+} migration along the Oh(Ni) $\rightarrow V_O \rightarrow$ Oh(Li) path.[67] Recent studies also found that the consecutive transformations from $Ni(OH)_6$ to NiO_6 octahedra *via* asymmetric and symmetric NiO_{6-x} octahedra take place during the growth of high nickel NCM, which also governs the Ni/Li ordering process in the layered structure.[81]

4.2 Side reactions at high voltage and temperature

The operating voltage window is one of the key parameters to determine the charge storage capacity of LIBs. A wider voltage window offers higher specific capacity and energy density. However, in the case of high Ni-NCM-based cathode materials, the higher cut-off voltage creates several issues like cation mixing, structural degradation, increase in O_2 release, *etc.* which deteriorate the overall electrochemical performance of the LIBs. The higher cut-off voltage also causes solid-electrolyte interface (SEI) formation on the anode, which has some positive impact on the stability of the anode and hence improved cycling performance. On the other hand, the adverse effect of SEI formation is that it hinders the stripping–plating of Li^+ on the anode. A summary of the effects of high voltage charging through the flow chart is given in Fig. 11a. Several research groups are trying to understand the effect of high voltage charging on Ni-rich NCM materials in terms of the structure and performance by various means, such as theoretical modelling, detailed *in situ* characterization, *etc.*[82–90] Manthirum and co-workers have experimentally demonstrated how a higher charging voltage adversely affects the cycling performance of NCM811-based LIBs.[86] It was observed from the cycling profile that the retention of the specific capacity of the pouch cell deteriorates from 72 to 52 to 38% as the higher cut-off voltage increases from 4.2 to 4.4 to 4.5 V. The lower cut-off is fixed at 2.5 V for all the cases. According to XRD (Fig. 11b) and FESEM (Fig. 11c), the structural degradation and phase change of the

cathode are the primary reasons for the performance degradation upon cycling. From the characterization data it was found that, at 4.2 V the cathode material almost retains its original quality, except a minute amount of electrolyte oxidation, cation mixing and cracking, whereas, in higher voltage ranges, *i.e.* at 4.4 and 4.5 V, the degree of oxidation, cation mixing and cracking were intensified along with severe phase change to NiO, TM-dissolution and crossover to the anode, leading to capacity fading. A similar result is also observed in the case of a $LiNi_{0.6}Co_{0.2}Mn_{0.2}O_2$-based cathode.[85] The discharge capacity of the cell increases from 176.0 mA h g^{-1} to 218.1 mA h g^{-1} at 1C with the increase in cutoff voltage from 4.3 V to 4.7 V, whereas the capacity retention decreases from 96.3% to 78.9% after 50 cycles, respectively. From impedance analysis it was observed that at 3.0–4.3 V, the R_{sl} value slightly increases to 18.7 Ω after 25 cycles, whereas it increases to 23.4 Ω and 28.2 at higher cut off voltages of 4.5 V and 4.7 V (Fig. 11d).[85] At the higher cutoff voltages of 4.5 V or 4.7 V, the cathode stays in the highly delithiated state, which triggers the migration of transition metal ions into Li layers, and causes lattice deformation of the cathode. This ion rearrangement hinders the Li^+ diffusion by decreasing the active sites for Li^+ intercalation.

Similar to the wide voltage window, a wider safe operating temperature range is also desirable for commercial applications. Most of the LIBs are presently limited to room temperature operations and high temperature operation causes several issues, which hampers the battery performance. Research is going on worldwide to address these issues.[91–94] Fig. 12a shows the major problems, caused due to the elevation of operating temperature in high Ni-content NCMs, such as deposition of TMs on the anode, reaction at the electrode and electrolyte interface and release of gases, which not only cause the performance fading of the battery but also lead to the thermal runaway and explosion of the cells. Recently, Wu *et al.* have demonstrated the heat release mechanism for the thermal runaway of NCM811-based high-energy lithium-ion batteries by using several characterization techniques, such as XRD, XPS, SEM and EDS.[91] According to their findings, within the temperature range of 1000–1600 °C the Al from the current collector and $Li_\alpha MO_x/MO_x$ (M = Ni, Co, Mn) from the cathode undergo the following transmetalation reaction:

$$Li_\alpha MO_x + Al \rightarrow MAl_yO_z + LiAlO_2 + Al_2O_3 + M \quad (7)$$

Within the 1000–1200 °C range:
In the case of $Li_\alpha MO_x$ the reaction is:

$$LiMO_x + Al \rightarrow LiMAl_yO_z + LiAlO_2 + M \quad (8)$$

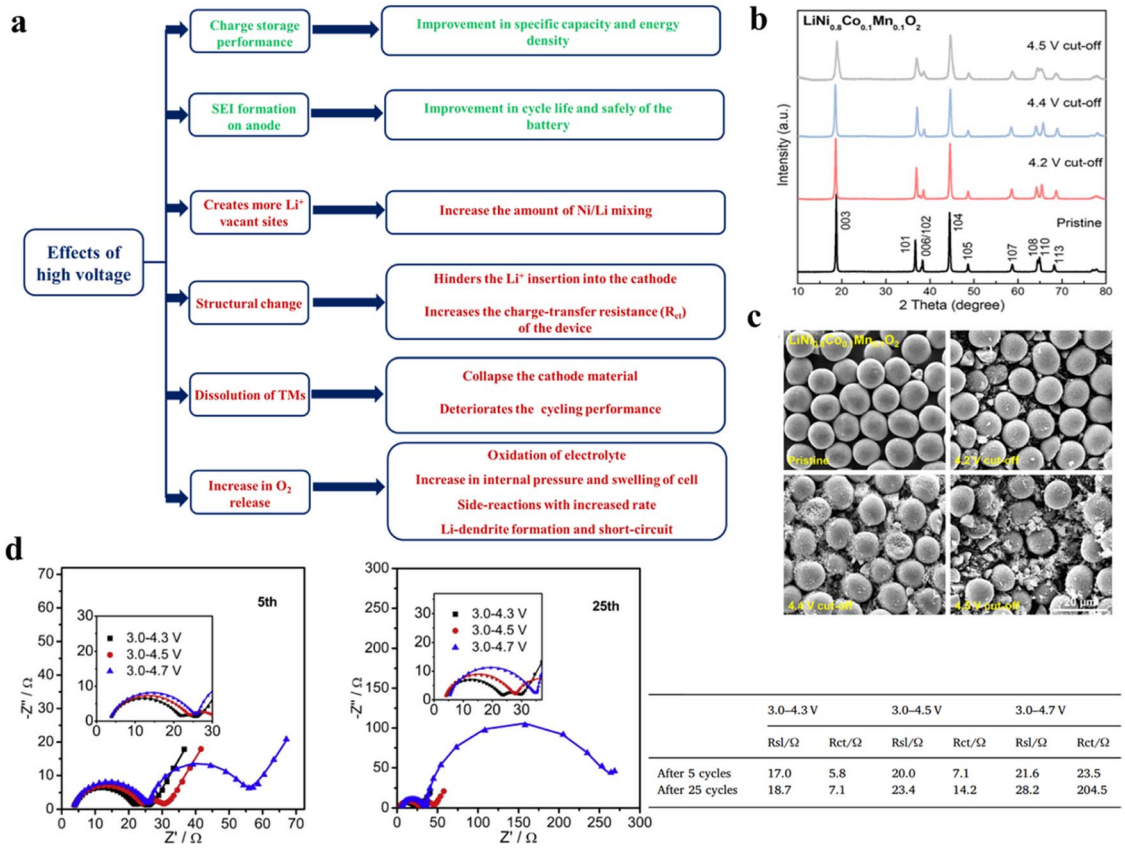

	3.0–4.3 V		3.0–4.5 V		3.0–4.7 V	
	Rsl/Ω	Rct/Ω	Rsl/Ω	Rct/Ω	Rsl/Ω	Rct/Ω
After 5 cycles	17.0	5.8	20.0	7.1	21.6	23.5
After 25 cycles	18.7	7.1	23.4	14.2	28.2	204.5

Fig. 11 (a) Effects of high voltage charging on high Ni-content cathodes. Post-cycling (b) powder XRD patterns and (c) SEM images of NCM811 after 1000 cycles (adapted with permission.[86] Copyright 2020, American Chemical Society). (d) Nyquist plots of $LiNi_{0.6}Co_{0.2}Mn_{0.2}O_2$ after 5 and 25 cycles. The fitted EIS data are given in a tabular form (adapted with permission.[85] Copyright 2018, Elsevier.).

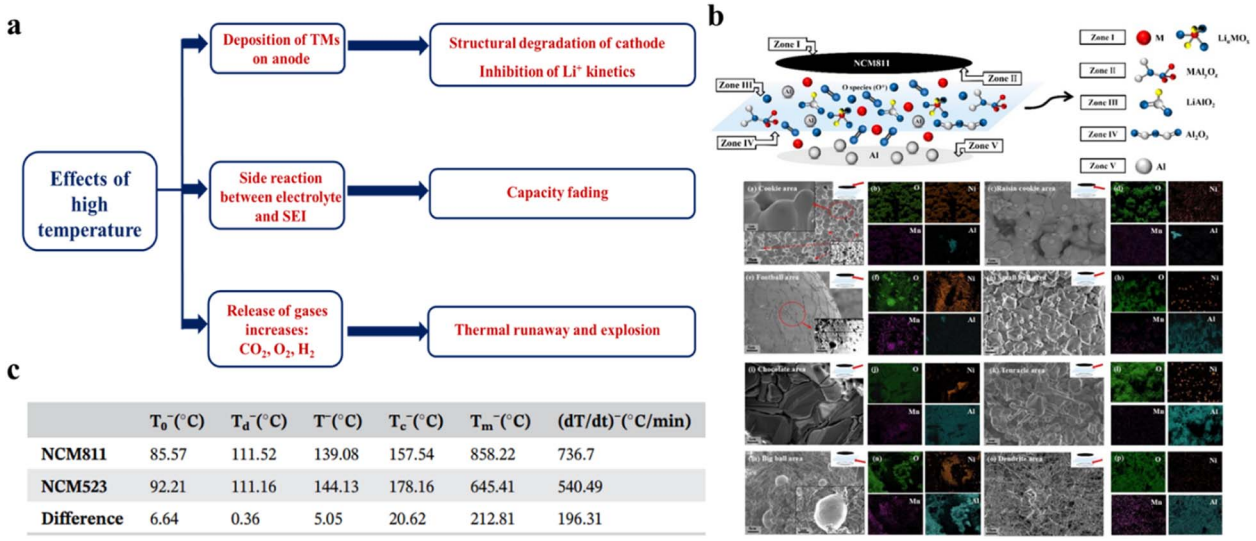

	T_0 (°C)	T_a (°C)	T (°C)	T_c (°C)	T_m (°C)	(dT/dt) (°C/min)
NCM811	85.57	111.52	139.08	157.54	858.22	736.7
NCM523	92.21	111.16	144.13	178.16	645.41	540.49
Difference	6.64	0.36	5.05	20.62	212.81	196.31

Fig. 12 (a) Effects of high temperature on high Ni-content cathodes. (b) SEM and EDS test results after high temperature heating of NCM811 (adapted with permission.[91] Copyright 2022, Elsevier.). (c) The average characteristic temperature of the NCM811 and NCM523 batteries in a tabular form (adapted with permission.[92] Copyright 2020, Wiley-VCH.).

In the case of MO_x the reaction is:

$$MO_x + Al \rightarrow MAl_yO_z + Al_2O_3 + M \quad (9)$$

Within the 1200–1600 °C range:

$$MAl_yO_z + Al \rightarrow Al_2O_3 + M \quad (10)$$

Based on SEM and EDS analyses, the surface morphology of the heated cathode (at 1600 °C) can be classified into six zones, given in Fig. 12b.[91] The replacement of the Al current collector may solve those issues. Wang *et al.* have compared the thermal runaway (TR) characteristic parameters for NCM811 (cylindrical batteries) and NCM523 (commercialized battery) at the 100% state of charge (SOC).[92] Fig. 12c shows the quantitative idea about those parameters. It is observed that the TR characteristics become more inconsistent as the Ni content increases.

4.3 Microcrack formation

The formation of microcracks upon cycling is one of the burning issues for Ni-rich cathode materials.[95] Dokko *et al.* have first identified the formation of microcracks in $LiNiO_2$-based cathodes due to volume change, induced by potential cycling induced consecutive Li^+ insertion/extraction upon discharging and charging by *in situ* optical microscopy.[96] The primary reasons behind the microcrack formation are the change of lattice parameters, phase transition from H2 to H3, range of depth of discharge (DOD), amount of oxygen release, *etc.*[95] The formation of micro-cracks on the surface of secondary particles offers more active sites to react with the electrolyte, leading to the dissolution of the cathode material as well as decomposition of the electrolyte. The microcracks further propagate towards the bulk upon repeated cycling and completely collapse the secondary particles, which severely affects the cycling performance of the battery. It is observed that the extent of microcracks increases with the range of DOD. According to the findings of Park *et al.* a Ni-rich $Li[Ni_{0.95}Co_{0.04}Al_{0.01}]O_2$ cathode shows a capacity retention of 60, 85.5 and 96.1% when cycled at an upper DOD of 60% (3.76–4.3 V), a lower DOD of 60% (2.7–4.0 V) and a DOD of 100% (2.7–4.3 V), respectively (Fig. 13a).[97] It is also observed that the extent of microcrack formation is also high at the upper DOD (Fig. 13b). In the case of high Ni-content (Ni > 0.8) NCM particles, repeated contraction and expansion during cycling at the charge/discharge end initiate the

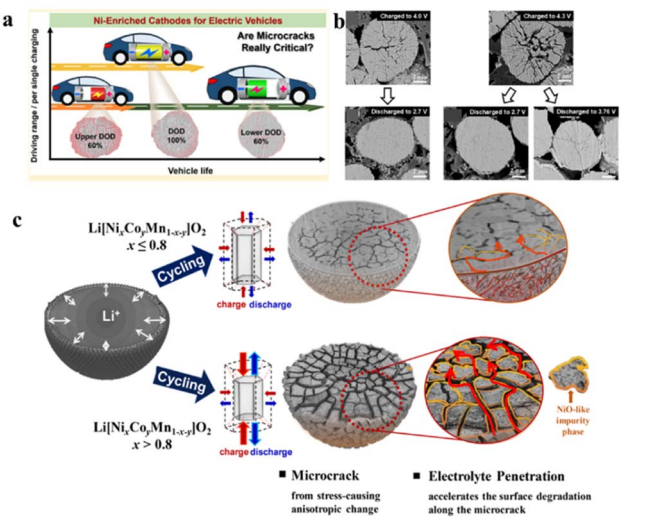

Fig. 13 (a) Variation of microcrack formation with the depth of discharge and (b) cross-sectional SEM images of NCA95 cathodes in the first cycle of different charged and discharged states (adapted from ref. 97). (c) Schematic representation of capacity fading of Ni-rich $Li[Ni_xCo_yMn_{1-x-y}]O_2$ cathodes due to microcrack formation (adapted with permission.[98] Copyright 2018, American Chemical Society).

microcrack formation and the presence of a high content of reactive Ni^{4+} further facilitates the propagation of microcracks by increasing the susceptibility towards reaction with the electrolyte (Fig. 13c).[98]

4.4 Lattice oxygen escape and phase transition

Phase transition caused by lattice oxygen escape is one of the bottlenecks for Ni-rich NCMs. The high calcination temperature and high upper cut-off voltage are the two primary reasons for the oxygen loss from the NCM structure, as already discussed in the previous section. The higher calcination temperature can also lead to small amounts of lithium loss from NCM. To compensate for the lithium loss, typically 3–5% excess lithium is always used during the synthesis of NCM cathode materials. Processing in oxygen is also necessary to avoid any reaction of NCM with air. It is also recommended that NCM cathode materials should not be kept in air. The starting precursor purity is also important for preparing high quality NCM cathode materials. It is observed that at a highly delithiated stage (voltage > 4.4 V), O^{2-} oxidation is more favored compared to transition metal oxidation.[99,100] At this stage, the highly reactive Ni^{4+} of the Ni-rich NCM moiety reduces to Ni^{2+} by oxidizing the electrolyte. In order to maintain the charge neutrality, the lattice O^{2-} oxidizes and escapes from the NCM lattice.[101] The released singlet oxygen ($^1O_2$) further facilitates electrolyte oxidation.[102] Thus, the release of lattice oxygen creates oxygen vacancies in the NCM crystal structure and promotes the migration of TMs from the tetrahedral to the octahedral site of the Li-slab.[103,104] The release of lattice oxygen in a higher amount at the highly delithiated stage causes stepwise phase transition from MO_2 (layered) → M_3O_4 (spinel) → MO (rock-salt) (Fig. 10a). The lattice oxygen release exacerbates the particle cracking related issue, which deteriorates the capacitive as well as cycling performance of Ni-rich cathodes.[105,106] Cation doping and interface engineering are two of the efficient strategies to prevent the lattice oxygen escape.[100,107,108]

5 Strategies to improve the electrochemical performance

High Ni-content NCMs, specifically NCM-811, would be a potential cathode material for the production of commercial high energy Li-ion batteries only if the issues can be addressed rationally. Several efforts and scientific advancements are in progress worldwide to improve the LIB performance in terms of specific capacity, energy density, rate capability and cycling stability.[109] A few of the promising aspects are discussed in this section.

5.1 Surface modification and protective coating

Protective coating of NCM-based cathode materials offers high mechanical stability, improves the Li^+ diffusion kinetics and protects the material surface from parasitic reactions with the electrolyte. The major parasitic reaction involves a spontaneous reaction between the surface-residual $LiOH/LiCO_3$ and the electrolyte ($LiPF_6$) to form an insulating layer of LiF on the cathode surface through the following reaction:[110–112]

$$LiPF_6 + Li_2CO_3 \rightarrow POF_3 + CO_2 + 3LiF \quad (11)$$

$LiPF_6$ also has a tendency to dissociate in the presence of moisture and generate HF through the following steps:[113]

$$LiPF_6 \rightarrow LiF + PF_5 \quad (12)$$

$$PF_5 + H_2O \rightarrow POF_3 + 2HF \quad (13)$$

$$POF_3 + Li_2O \rightarrow 6LiF + P_2O_5 \quad (14)$$

The *in situ* generated HF also corrodes the material surface and affects the structural integrity of the cathode. Surface coating is an effective strategy to protect the NCM surface from direct contact with the electrolyte. The coating layers can be classified into: (i) metal oxides; (ii) phosphides and fluorides; (iii) Li-containing compounds; (iv) conducting polymers and carbon.

5.1.1 Metal oxides. There are a number of reports, which demonstrated that coatings with various metal oxides such as WO_3, TiO_2, Y_2O_3, MoO_3, ZnO, ZrO_2, MgO, and Al_2O_3 act as efficient protective layers for high-Ni NCMs and improve the electrochemical performance.[114–121] Becker *et al.* have coated NCM-811 with a WO_3 layer through the sol–gel technique and experimentally proved that the coated material possesses improved mechanical and thermal stability and also better cycling performance at different cut off voltages.[118] From post-cycling SEM images (Fig. 14a–c), it is observed that the coated electrodes are free from severe cracking as the WO_3 layer protects the surface of the NCM from close contact with the electrolyte and thus ceases the formation and propagation of microcracks from the surface to the core of the secondary particles. Similarly, an Al_2O_3 coating of <5 mm on NCM-622 was also found to be beneficial in terms of improved rate capability and cycling performance in the higher range of upper cut off voltages.[121] In the case of ZnO coating, it is observed that although it is efficient in mitigating the cathode dissolution and protecting the surface from HF attack, the poor conductivity of ZnO causes increased polarization of the electrodes.[122] In order to improve the conductivity of the ZnO layer, Al_2O_3 was doped into it (abbreviated as AZO) and first used as the coating layer of $LiCoO_2$ in 2015.[122] Recently, Zhang *et al.* have utilized AZO as an efficient surface protector of NCM-811 by simple wet-mixing of AZO dispersion of ethanol ($ZnO : Al(OH)_3 = 99 : 1$) with NCM-811 followed by drying and calcination at 500 °C for 5 h.[123] The AZO-coated NCM-811 shows higher specific capacity as well as longer cycling stability within the voltage window of 3.0 to 4.5 V. Moreover, it is observed from impedance analysis that the charge transfer resistance (R_{ct}) is less for the coated material (Fig. 14d), indicating facile Li^+ diffusion kinetics.[123] Poor conductivity is one of the primary concerns about oxide coating.[124,125]

5.1.2 Phosphides and fluorides. Metal phosphides, such as $ZrPO_4$, $LaPO_4$, $MnPO_4$, $AlPO_3$, $MgHPO_4$ and $LiPO_4$, are widely used as efficient protective layers for high-Ni NCMs.[126–133] The

$LiPO_4$ coating is discussed under the subheading of "Li-containing compounds". $LaPO_4$-coated NCM811 shows a higher percentage of capacity retention and smaller charge transfer resistance compared to the uncoated one.[127] Similar results are also obtained for $Al(PO_3)_3$ coated NCM811.[128] There is also a report on organic phosphates, such as dihexadecyl phosphate coating on NCM811. Here the outer alkyl surface, being hydrophobic in nature, is helpful in attenuating the effect of H_2O/CO_2 on the particle surface and the O=POLi containing inner layer facilitates the Li^+ transport. Xie *et al.* have studied the effect of fluoride coating with different fluorides on the structural stability of NCM-523.[134] An AlF_3-coated NCM-523 cathode shows a greater percent of capacity retention of 88% after 200 cycles with a higher cut-off voltage of 4.5 V, compared to the CeF_3-coated NCM-523 cathode with only 60% (higher cut off is 4.3 V). It is claimed that the fluoride coating protects the cathode-electrolyte interface by maintaining the pH at 4.0 and small metal cationic radius.

5.1.3 Li-containing compounds. Li-containing conducting compounds are preferable as the coating layer for high-Ni NCMs as it protects the surface from the adverse effect of the electrolyte without hampering the Li^+ diffusion kinetics. The $LiPO_4$ coating plays the role of a scavenger of both residual water and HF in the electrolyte through the reactions (15) and (16):[135,136]

$$Li_3PO_4 + H_2O = Li_xH_yPO_4 \text{ (or } PO_xH_y) + Li_2O \quad (15)$$

$$Li_3PO_4 + HF = Li_xH_yPO_4 \text{ (or } PO_xH_y) + LiF \quad (16)$$

There are several reports on the $LiPO_4$ coating for high-Ni-content NCMs, which shows improved cycling performance and Li^+ diffusion behavior compared to the uncoated materials.[122,124,126] Other lithium containing compounds, such as $Li_4Ti_5O_{12}$, $Li_{1.4}Al_{0.4}Ti_{1.6}(PO_4)_3$, $Li_{1.8}Sc_{0.8}Ti_{1.2}(PO_4)_3$, Li_2CO_3/$LiNbO_3$, *etc.*, are also utilized as the coating material for high-Ni content NCMs.[137–140] Fan *et al.* have coated $Ni_{0.60}Co_{0.10}Mn_{0.30}(OH)_2$ precursors with $Li_{1.8}Sc_{0.8}Ti_{1.2}(PO_4)_3$ by following three steps: (i) preparation of an ethanolic solution of $LiNO_3$, $Sc(NO_3)_3 \cdot H_2O$, and H_3PO_4 (molar ratio of Li : Sc : P = 1.8 : 0.8 : 3) and a stoichiometric ratio of $Ti(C_4H_9O)_4$, (ii) addition of the spherical hydroxide precursor into the solution and mixing with mild stirring to obtain LSTP precursor@ $Ni_{0.60}Co_{0.10}Mn_{0.30}(OH)_2$ and (iii) mixing of LSTP precursor@ $Ni_{0.60}Co_{0.10}Mn_{0.30}(OH)_2$ with $LiOH \cdot H_2O$ (Li : M ratio = 1.06 : 1) and calcinating in

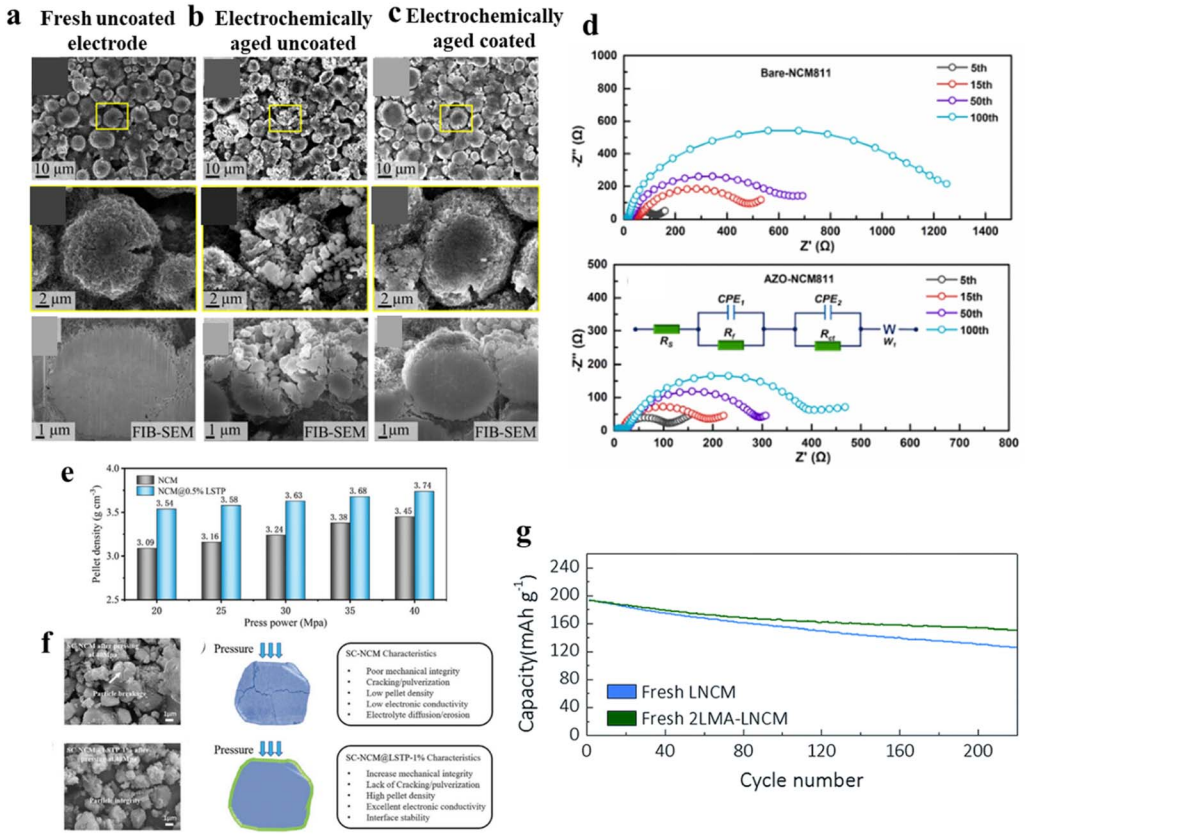

Fig. 14 SEM images of the surface and cross section of the (a) fresh uncoated NCM-811 electrode, (b) electrochemically aged uncoated NCM-811 electrode (after 465 cycles; SOH = 80%), and (c) electrochemically aged tungsten oxide-coated NCM-811 electrode (after 867 cycles; SOH = 80%) (adapted with permission.[118] Copyright 2019, American Chemical Society), (d) Nyquist plots of bare-NCM811 and AZO-NCM811 (adapted with permission.[123] Copyright 2022, Elsevier.), (e and f) mechanical strength characterization of SC-NCM and SC-NCM@LSTP-1% and schematics of after pressing and characteristics (adapted with permission.[139] Copyright 2022, Wiley-VCH.) and (g) cycle performance of fresh LNCM and 2LMA-LNCM between 3.0 and 4.5 V at a C/3 rate (adapted with permission from ref. 141. Royal Society of Chemistry).

two steps, such as at 550 °C followed by 930 °C for 10 h in an oxygen atmosphere to obtain the final product termed single crystal $Li_{1.8}Sc_{0.8}Ti_{1.2}(PO_4)_3$ coated $Ni_{0.60}Co_{0.10}Mn_{0.30}(OH)_2$ [SC-NCM@LSTP].[139] The particle density is higher for SC-NCM@LSTP compared to bare SC-NCM (Fig. 14e). Moreover, LSTP-coating enhanced the physical and chemical properties and thus improved the mechanical stability of the material (Fig. 14f). The surface modification provides the material with a higher cut-off voltage of 4.6 V with improved rate capability and cycling performance. In another report, Xu *et al.* have experimentally proved that 1 wt% $Li_4Ti_5O_{12}$ coating is beneficial for the improved capacity retention of NCM-811 as it not only facilitates the Li^+ diffusion but also efficiently suppresses the parasitic side reactions on the material surface.[137] The coated material shows a capacity retention of 75.86% at 1C after 170 cycles within the voltage range of 2.7 and 4.3 V at 25 °C, which is far better than the bare one (39.40%). As it is recognized that Mn-rich spinel oxides have good chemical stability upon exposure to ambient air than high-Ni-content NCMs, Manthiram *et al.* utilized a Mn-rich spinel oxide of $LiMn_{1.9}Al_{0.1}O_4$ to coat high-Ni-content NCMs.[141] A high capacity retention of 80% for 200 cycles has been achieved for the 2 wt% $LiMn_{1.9}Al_{0.1}O_4$-coated $LiNi_{0.7}Co_{0.15}Mn_{0.15}O_4$ (2LMA-LNCM) sample, as compared to that of 68% for the pristine LNCM sample (Fig. 14g).[141] They also demonstrated that the loss of battery performance of high-Ni-content NCMs due to long-term storage in air could be restored by heat treatment above 400 °C.[141] Alternatively, Sun *et al.* demonstrated that the treatment of high-Ni-content NCMs in a solution of 2.0 m lithium bis(-fluorosulfonyl)imide (LiFSI) dissolved in dimethyl carbonate (DMC) at 60 °C for 24 hours can also restore and improve its cycling performance.[142] It showed that the treatment in LiFSI/DMC solution led to the conversion of surface alkaline species such as Li_2O, LiOH and Li_2CO_3 to LiF, which is a more stable and essential component of the cathode electrolyte interphase (CEI), resulting in improved cycling performance.[142] Zhang et al. coated the NCM811 surface with Li_3PO_4–LiF by vigorous ball milling of the NCM811-$LiPF_6$ (0.5–2.0 wt%)-*N*-methyl pyrrolidinone (NMP) suspension for 75 min, which not only improved the cycling stability but also enhanced the rate capability of Li/NCM811 cells.[143]

5.1.4 Conducting polymers and carbon. Conducting coating layers, such as polymers and carbon, are advantageous as they simultaneously promote facile Li^+ diffusion kinetics as

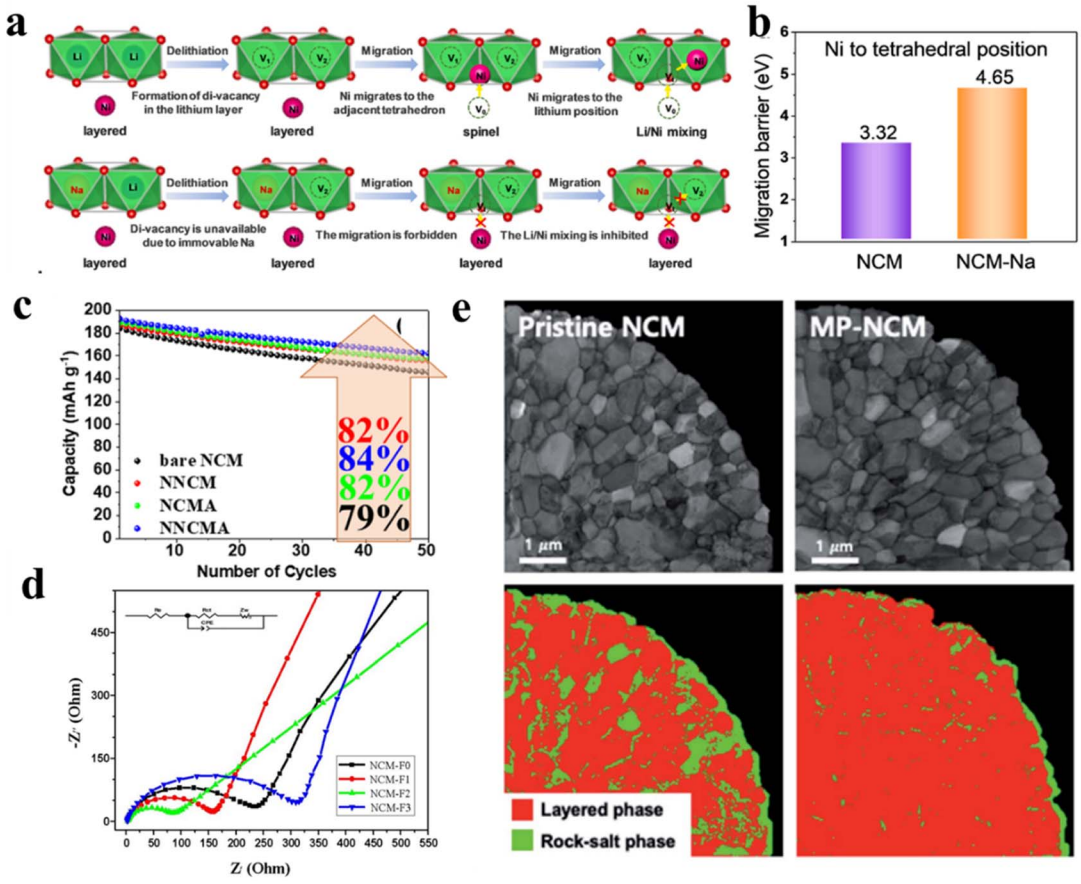

Fig. 15 (a) Schematic representation of inhibition of phase transition and Li^+/Ni^{2+} mixing by Na doping and (b) migration barrier in Na-doped and undoped NCM (adapted with permission.[36] Copyright 2022, Elsevier.), (c) cycling performance of NCM, NNCM, NCMA, and NNCMA during the 50th cycle at 1C and room temperature (adapted with permission.[155] Copyright 2022, American Chemical Society), (d) EIS curves of NCM with various F^- doping (adapted with permission.[157] Copyright 2022, Wiley-VCH.) and (e) ASTAR TEM phase mapping analysis and bright-field TEM images of pristine NCM and Mg-phosphate-doped/coated-NCM (MP-NCM) (adapted with permission from ref. [130], Royal Society of Chemistry).

well as high mechanical strength of the NCM. Conducting polymers, like polypyrrole, polyaniline, *etc.*, are used as the coating layer for high Ni-content NCMs.[144,145] It is observed that 3 wt% PANI-coated $LiNi_{0.8}Co_{0.1}Mn_{0.1}O_2$ exhibits a higher capacity retention of 96.25% after 80 cycles at a current rate of 1C and 83.02% retention at 5C, which is better than the uncoated material. The polymer layer is helpful in suppressing the side reaction, improves the electronic conductivity and increases the extent of redox reactions. Similarly, an amorphous carbon coating improves the cycling performance and rate capability of high Ni-NCM.[146] It is found that the effect of the carbon coating largely depends on the thickness of the coating layer, which is tunable by controlling the calcination temperature.

5.2 Cation/anion doping

The doping of ions is proved to be a fruitful strategy to change the electronic configuration locally and improve the overall conductivity of the material. Cation doping is also helpful in mitigating transition metal dissolution-related issues.[147] Various cations, such as Na^+, K^+, Mg^{2+}, Al^{3+}, Nb^{5+}, V^+, W^{6+}, Mo^{6+}, Zr^{4+}, Si^{4+}, *etc.*, are successfully doped into the crystal moiety of high Ni-NCMs/NCAs to improve the structural stability, conductivity and electrochemical performance.[148–154] Shen *et al.* have doped $Ni_{0.6}Co_{0.05}Mn_{0.35}O_2$ with varying amounts of Na^+ and K^+ (1–3%) and evaluated the electrochemical performance.[36] It was observed that 2% Na^+ and 1% K^+ doping could efficiently improve the performance individually. In the case of $Li_{1-x}Na_xNi_{0.6}Co_{0.05}Mn_{0.35}O_2$ (NCM-Na), Na^+ plays a crucial role in preventing Li^+/Ni^{2+} mixing to a large extent by creating an electromagnetic barrier. The schematic illustration, describing the role of Na^+ doping, is given in Fig. 15a and b.[36] This leads towards improved cycling performance even at a high voltage of 4.5 V and good rate capability at 3C for Na-doped NCM. Mg^{2+}-doped high Ni-NCMs, such as $LiNi_{0.80}Mn_{0.10}Co_{0.10}O_2$, $LiNi_{0.90}Mn_{0.05}Co_{0.05}O_2$, $LiNi_{0.91}Co_{0.06}Mn_{0.03}O_2$, *etc.*, show improved cycling as well as rate performance.[28,131] Mg doping efficiently prevents microcrack formation and improves the structural robustness. The larger size of Mg^{2+} also works as a pillar between the two consecutive layers of the NCM and provides phase stability by screening the O^{2-} O^{2-} repulsion during the charging step.[131] In the case of Al-doping, a prominent improvement is observed in the thermal stability and the hardness of NCM-811 compared to the unmodified one.[154] Zhang *et al.* have evaluated the effect of Nb^{5+}, Sr^{5+} and Y^{3+} doping into NCM-712 and further focus on the effect of Nb^{5+} on the structural stabilization.[30] Nb^{5+} doping efficiently mitigates the Ni^{2+}/Li^+ mixing and facilitates the Li^+ diffusion. The dual doping of cations synergistically improves the quality as well as the electrochemical performance of NCM-based cathodes. Recently, Park *et al.* have doped $LiNi_{0.88}Co_{0.08}Mn_{0.04}O_2$ with Na^+/Al^{3+} and evaluated the effect of change in lattice parameters on the cycling performance of the material.[155] Singly doped and dual doped materials are synthesized by sintering bare NCM with LiOH, NaOH, and $Al(NO_3)_3 \cdot 9H_2O$ at 500 °C for 5 h and then at 750 °C for 12 h in an O_2 atmosphere followed by cooling to room temperature. The as-synthesized materials are termed NCMA [$Li(Ni_{0.88}Co_{0.08}Mn_{0.04})_{0.995}Al_{0.005}O_2$], NNCM [$Li_{0.995}Na_{0.005}(Ni_{0.88}Co_{0.08}Mn_{0.04})$–$O_2$] and NNCMA [$Li_{0.995}Na_{0.005}(Ni_{0.88}Co_{0.08}Mn_{0.04})_{0.995}Al_{0.005}O_2$]. NNCMA shows better capacity retention (84%) compared to bare and singly doped materials after 50 charge–discharge cycles at 1C within the voltage range of 2.8–4.35 V (*vs.* Li/Li^+), as shown in Fig. 15c.[155] The reason behind the improved cycling performance can be described by the modified crystal structure of NNCMA. Here, the bigger-sized Na^+ occupies the Li^+ sites and expands the Li-slabs, leading to the improved diffusion kinetics of Li^+. On the other hand, transition metal sites are occupied by the comparatively less electronegative Al^{3+}, resulting in a decrease in TM sites. Thus, the dual doping offers a stabilized and ordered crystal structure with less cation mixing. Among the non-metals, boron doping helps in capacity retention upon long-term cycling in high Ni-content NCMs. It is observed that the boron doping on the agglomerated surface prevents cation disorder and phase transition leading to improved cycling performance. However, boron doping in bulk adversely affects the electrochemical performance of the material.

The modification of the crystal structure of high Ni-content NCMs with anion doping, such as fluorine, nitrogen, borates, *etc.*, plays a crucial role in facilitating the Li^+ diffusion kinetics. Fluorine doping is beneficial in terms of two aspects: (i) it replaces the less electronegative O^{2-} ions and decreases the extent of oxygen release and thus improves the coulombic efficiency; (ii) F^--doping effectively reduces the Jahn–Teller distortion in Mn^{3+} by increasing the average valence state of Mn and thus provides longer cycling stability.[156] Huang *et al.* have reported that a moderate amount of F^--doping decreases the charge-transfer resistance (Fig. 15d) and improves the reversibility of Li^+ intercalation/de-intercalation.[157] The incorporation of borates $(BO_3)^{3-}$ and $(BO_4)^{5-}$ also provides structural stability to lithium-rich manganese oxides.[158,159]

5.3 Dual modification with doping and coating

Dual modification with surface coating and bulk doping synergistically improves the NCM performance in terms of structural stability and electronic conductivity. A few of the recent literature studies describe the benefits of dual modification in achieving high specific capacity as well as longer cycle life.[130,131,160–162] Hwang *et al.* have modified NCM-811 with Mg doping and $LiPO_4$ coating by calcinating a NCM and $MgHPO_4 \cdot 3H_2O$ mixture at 750 °C for 15 h in air followed by mixing Mg-doped NCM811 with polyphosphoric acid (PPA, 0.4 g) into dimethyl sulfoxide (DMSO, 10 g).[130] From ASTAR TEM analysis (Fig. 15e), it is clearly observed that the Mg-doping and $LiPO_4$ coating on NCM811 synergistically prevent the transformation from a layered structure to a rock salt phase above 4.2 V *vs.* Li/Li^+, which offers a better cycle life with good rate capability of the modified material compared to pristine NCM811. Starrar *et al.* have performed a similar kind of modification for $LiNi_{0.91}Co_{0.06}Mn_{0.03}O_2$ through a single step calcination process. The dual-modified NCM shows an improved Li^+ diffusion co-efficient due to the presence of a Li-containing

conductive coating layer.[131] Various combinations of coating layers, such as Li_2ZrO_3, B_2O_3, Li_2WO_4, WO_3, *etc.*, with Zr-doping also improve the structural stability and electrochemical performance of high-Ni containing materials.[161,162] Gao *et al.* have achieved the dual modification of Zr-doping and Li_2ZrO_3 coating on NCM-811 (Zr-NCM811) by the sol–gel method. First an aqueous solution of transition metal nitrate precursors and $LiNO_3$ is mixed with a water : ethanol = 1 : 1 solution of $Zr(C_5H_7O_2)_4$ to achieve $Li_{1.05}(Ni_{0.8}Co_{0.1}Mn_{0.1})_{1-x}Zr_xO_2$, where x = 0, 0.005, 0.01, 0.02, 0.05, respectively.[160] Then, a gel was prepared by mixing the as-prepared solution with citric acid solution, followed by addition of added $NH_3 \cdot H_2O$ and heating it at 90 °C under stirring for 15 h. $NH_3 \cdot H_2O$ helps to keep the pH within 7.0–7.2. The gel was baked at 150 °C for 24 h and further calcined at 480 °C for 8 h in air to get a dark brown colored powder, which was calcined at 900 °C for 15 h in oxygen to obtain the final cathode material. The Zr-doping and *in situ*-generated lithium zirconate coating benefit NCM811 in the following manner: (a) Zr^{4+} in the lattice stabilizes its layered structure by suppressing the layered to spinel transformation and also decreases the Li^+ diffusion energy barrier by expanding the lattice spacing; (b) the lithium zirconate coating layer simultaneously protects the NCM811 surface from the parasitic side reactions with the electrolyte and facilitates the Li-ion transport throughout the particles.

5.4 Synthesis of core–shell

The synthesis of core–shell structured NCMs is useful in terms of protecting the material core from the parasitic reactions of the electrolyte. Although similar results can be achieved by coating, getting a uniform coating layer is a delicate job. The core–shell structure is composed of two different materials with different crystal structures. In the case of high Ni-content NCMs, the primary target is to make a Ni-rich core to achieve high specific capacity, whereas the shell will provide structural robustness during long-term cycling performance. Although the shell material is required to be chemically inactive towards the electrolyte, it should provide appropriate channels for Li^+ diffusion into/from the core during the charge–discharge process. Several groups have developed unique core–shell structures keeping the Ni-rich component at the core in order to improve electrochemical performance.[163–166] Nathagopal *et al.* have synthesized nitrogen-doped carbon (NC) coated NCM-811 by a dry-solid state method using dopamine hydrochloride as the NC source and 0.2 wt% NC@NCM811 showed less charge transfer resistance in impedance analysis.[163] Lee *et al.* have synthesized a $[Ni_{0.85}Co_{0.10}Mn_{0.05}](OH)_2$ core with the shell of less Ni by leaching the as-synthesized hydroxide precursor with different concentrations of H_2SO_4.[164] It was observed that the product leached with 5 mol%H_2SO_4 is superior in terms of specific capacity, rate capability and cycling performance. However, as the sulfuric acid concentration was increased from 5 to 25 mol%, the rate capability of the material deteriorated, probably due to the increase of interfacial resistance caused by the increasing extent of cation mixing. A similar result is obtained when the core–shell structure of NCM-811 (CS-NCM811) was prepared by maintaining a higher Ni-content at the core ($Ni_{0.9}Co_{0.05}Mn_{0.05}(OH)_2$) and less Ni-content ($Ni_{0.4}Co_{0.3}Mn_{0.3}(OH)_2$) at the shell.[165] A higher I_{300}/I_{400} value (1.74) of CS-NCM811 compared to pristine NCM811 (1.42) indicates less cation mixing in the core–shell structure. The core–shell structure not only offers better electrochemical performance but also the Mn-rich shell improves the thermal stability of the whole material. In the case of core–shell NCMs, the core and shell have structural incompatibility and different extents of volume change upon cycling, which severely affects the structural robustness in the delithiation step.

5.5 Materials with concentration gradient

Concentration gradient, an advanced version of core–shell engineering, is the structure with smoothly varying concentrations of the different components throughout the material, which simultaneously offers high charge storage performance as well as good structural stability (Fig. 16a). It is already discussed in the previous sections that the Ni-rich core offers high specific capacity, the Mn-rich shell provides structural robustness and the presence of Co is essential to decrease the extent of cation mixing throughout the Ni-rich NCM-structure. Hence, proper control over the concentrations of the metal components within each particle (from the center towards the edge) is advantageous to achieve good battery performance even at higher C-rates. Several researchers have already attempted to synthesize Ni-rich NCM particles with concentration gradient and got promising results.[167–175] In general, NCM-811 with a full concentration gradient is synthesized by usual co-precipitation followed by a high-temperature lithiation step. Unlike the usual process, in this case the total metal-concentration (required to form NCM-811) is divided in several parts, containing varying Ni, Co and Mn and is fed to the reactor using multiple pumps at the same time. Jiang *et al.* have used 2 mol L^{-1} $NiSO_4$ and $CoSO_4$ solution (solution A) and 2 mol L^{-1} $MnSO_4$ solution (solution B) to synthesise NCM-811 with concentration gradient.[167] They achieved a relative molar content of 88% of Ni at the center and 72% at the edge of the spherical NCM-811 hydroxide precursor particle, whereas the relative content of Mn increases gradually from the center to the edge. After lithiation at 800 °C the concentration gradient of Ni becomes slightly slower (84% at the center and 76% at the edge) due to the thermal diffusion of the ions during calcination. The full-gradient material exhibits good cycling stability of 90% capacity retention after 100 cycles at a 5C rate, which is higher than that of the material without gradient with 71.8% capacity retention. Xu *et al.* have synthesized $LiNi_{0.7}Co_{0.13}Mn_{0.17}O_2$ with full concentration gradient by feeding a Ni-poor metal salt solution (Ni : Co : Mn = 5 : 2 : 3, 240 mL, and 2 mol L^{-1}) into a Ni-rich (8 : 1 : 1, 80 mL, and 2 mol L^{-1}) solution.[168] The material with concentration gradient not only shows a higher specific capacity of 189.9 mA h g^{-1} at 0.1C but also a capacity retention of 86.5% after 300 cycles at 1C. It is also observed from the cyclic voltammetry profile that the peak, corresponding to the H2 to H3 transition above 4.2 V, is depressed in the case of the gradient material compared to unmodified NCM-811. This signifies that the gradient structure

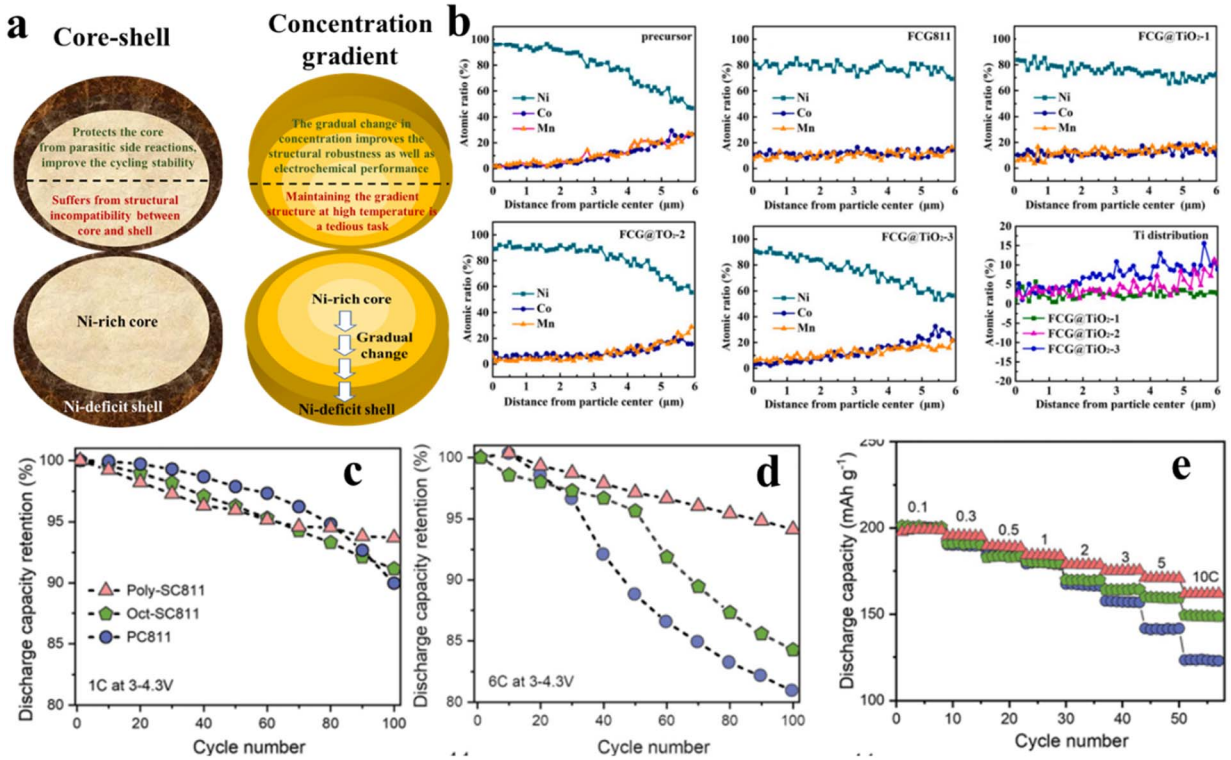

Fig. 16 (a) Schematic illustration demonstrating the difference between the core–shell and concentration-gradient Ni-rich NCMs, (b) variation of concentration gradient upon TiO_2 incorporation within NCM811 particles both in precursor and lithiated stages (adapted with permission.[169] Copyright 2020, Elsevier.) and (c–e) comparison of the discharge capacity retention and rate capability of Poly-SC811, Oct-811 and PC811 (adapted with permission.[193] Copyright 2022, Wiley-VCH.).

successfully mitigates the phase transition and ceased the structural degradation of the cathode during Li-intercalation/de-intercalation. The tensile tangential stress is also markedly depressed at the surface of the NCM particles with concentration gradient. It is generally observed that, due to the interdiffusion of transition metals at high temperature, the concentration gradient becomes less prominent after high temperature calcination. Zhang *et al.* have synthesized $LiNi_{0.90}Co_{0.07}Mg_{0.03}O_2$ with the concentration gradient of Mg. The as-synthesized cathode shows promising rate capability and long cycling performance. Here, the Mg-poor core offers high capacity and the Mg-rich shell enhances the structural stability and improve the Li-ion diffusion kinetics.[174] In order to maintain the initially obtained gradient in the final calcined material, Mo *et al.* have incorporated TiO_2 into the NCM-811 structure.[169] First, NCM811 with concentration gradient was synthesized by the hydroxide co-precipitation method, feeding a 2.5 M $NiSO_4 \cdot 6H_2O$ solution followed by Ni-deficient solutions ($Ni:Mn = 5:1$ and $Ni:Co:Mn = 4:4:2$) into the reactor. NH_4OH and NaOH were used as the complexing and precipitating agents, respectively. To obtain the TiO_2 incorporated final material, the hydroxide precursor was mixed with LiOH and varying amounts of TiO_2 and calcined at 750 °C for 12 h. Fig. 16b describes the change in the concentration gradient of the components with different amounts of TiO_2 incorporation.[169] The precursor possesses a higher Ni content of 82% at the center and decreased to 72% at the edge and after lithiation the gradient becomes smoother in the case of NCM-811. However, in the case of TiO_2 incorporated NCMs the gradient remains intact throughout the materials. In this case, the formation of Li–Ti–O and Ti–O complexes effectively reduces the thermal diffusion of TM ions and maintains the integrity of the concentration gradient. On the other hand, partial Ti^{4+} doping also stabilizes the crystal structure of NCM-811. The TiO_2-incorporated NCM with concentration gradient shows better cycling performance and rate capability compared to the material without TiO_2. The electrochemical performance of Ni-rich cathodes is further improved when the benefits are obtained from simultaneous doping, coating and concentration gradient structure. There are a few recent reports where high Ni-content NCMs are synthesized with concentration gradient and their structural stability and electrochemical performance are further improved by doping of Nb, La, Al *etc.* and coating with $LiNbO_3$, La_2O_3, *etc.*[176,177]

5.6 Single crystal cathodes

In the case of polycrystalline Ni-rich cathodes, the secondary particles are composed of multiple randomly distributed primary particles. As a result, severe volume change and electrolyte penetration along the grain boundaries during charge–discharge cycles lead towards the cracking of both the primary and secondary particles.[178] One logical remedy for this issue is

to produce single crystal cathode materials made of a limited number of uniformly oriented primary micro-crystals. Generally, the co-precipitation-derived precursors are subjected to the calcination at a controlled temperature of ≥850 °C to obtain single crystal NCMs. However, in the case of Ni-rich NCMs the high calcination temperature leads to several issues, like increased extent of cation mixing, oxygen loss, phase transition, *etc.* The flux assisted synthesis method, where various molten salts are utilized during the calcination process, is found to be beneficial to decrease the calcination temperature and facilitate the regular orientation of primary particles.[179–183] The presence of surface impurities is one of the key issues for this process. Hence, other synthesis methods, including hydrothermal, sol–gel, template assisted synthesis, vapor-phase deposition method, spray pyrolysis, *etc.,* are also explored to produce single crystal Ni-rich NCMs.[66,68,128,184–189] Recently, several efforts have already been made to produce single crystal NCMs with a higher Ni-content and to compare the performance with the polycrystalline one.[190–202] As an example, Ran *et al.* have shown that single crystal NCM811 is superior in terms of cycling as well as rate performance compared to the polycrystalline one.[190] Recently, Kim *et al.* have synthesized three different single crystal high-Ni NCMs, having a similar particle size distribution and morphology, such as $LiNi_{0.8}Mn_{0.1}Co_{0.1}O_2$, $LiNi_{0.80}Mn_{0.15}Co_{0.05}O_2$, and $LiNi_{0.85}Mn_{0.10}Co_{0.05}O_2$ by the co-precipitation method in the presence of poly(vinylpyrrolidone) (PVP) followed by calcination and analyze their chemical, electrochemical and thermal properties.[191] From their study, it was observed that the presence of Ni^{3+} in higher amounts reduces the thermal and air stability of higher Ni-content single crystal NCMs, whereas Mn improves all kinds of stability. Unlike Ni, Co remains almost chemically inactive upon exposure to air. It is also important to mention in this context that the surface energy of the facets plays an important role in the reactivity of Ni-rich NCMs. From the *ab initio* study of Liang *et al.*, it was found that the order of the surface energy in NCM811 follows the given trend: (104) < (001) < (111) < (012) < (110) < (100).[192] Lu *et al.* have synthesized two different kinds of single-crystal NCM811, such as (i) octahedron-shaped NCM811 with a predominating (012)-family surface (Oct-SC811) and (ii) polyhedron-shaped NCM811 with a predominating (012)-family surface (Poly-SC811).[193] Oct-SC811 is synthesized by hydroxide co-precipitation followed by high temperature calcination at 930 °C with $LiOH \cdot H_2O$ under an oxygen flow. On the other hand, Poly-SC811 was synthesized by a hydrothermal method (carbonate co-precipitation) followed by calcination. From the cycling stability experiment, it was observed that Poly-SC811 shows better cycling stability under fast-charging conditions and good rate capability compared to Oct-SC811 and polycrystalline NCM811 (Fig. 16c–e).[193] It is also observed that the single-crystalline Ni-rich cathodes are almost free from oxygen-loss-related phase degradation.[201] Although single crystal NCMs are superior in terms of structural robustness and electrochemical performance, they still suffer from issues like interfacial defects, kinetic limitations and potential cycle-induced phase transition.[179] Similar to polycrystalline NCMs, cation doping and surface coating are also adopted to mitigate the issues in the case of single crystal NCMs.[203–205] Single crystal Ni-rich NCMs are also utilized to fabricate high performance solid state LIBs, which is discussed in a later part of the article. However, in the case of single crystal NCMs the Li^+ diffusion kinetics and thermal stability largely depend on the grain size of the material, which is further dependent on the specific reaction conditions and synthetic processes. Hence, the synthesis of single crystal Ni-rich NCMs in bulk is a delicate job and scientific efforts are in progress.

5.7 Electrolyte additives

Besides modification of cathode materials, it is more convenient to use electrolyte additives to improve the cycling stability of high Ni-NCMs. A small amount of additives has little influence on the ionic conductivity and viscosity of the state-of-the-art liquid electrolytes but can significantly improve the properties of the passivation layers at the cathode, resulting in significantly improved long cycling stability of batteries.[206–209] Battaglia *et al.* found that the addition of 1 vol% tris(-trimethylsilyl)phosphite (TMSPi) and 1 vol% vinylene carbonate (VC) to a standard electrolyte of 1.0 M $LiPF_6$ in a mixture of ethylene carbonate (EC) and dimethyl carbonate (DMC) (1 : 1 vol.) significantly increased the capacity retention of a NMC811/graphite full cell to 91% after 200 cycles at C/3, as compared to less than 30% for the baseline cell after 100 cycles.[210] Similar to other TMS terminated compounds,[207] TMSPi can act as an HF scavenger and reduces transition metal dissolution of NMC811 and improves its long cycling stability.[210,211] Zhang *et al.* demonstrated that 2 wt% lithium bis(oxalato)borate (LiBOB) as an additive could simultaneously stabilize the lithium anode and $LiNi_{0.76}Mn_{0.14}Co_{0.10}O_2$ (NMC76) cathode, achieving a capacity retention of 96.8% after 200 cycles at C/3, as compared with a capacity retention of 85.1% for the cell without LiBOB.[212] Li *et al.* further demonstrated that both 2 wt% LiBOB and lithium difluoro(oxalato)borate (LiODFB) can effectively enhance the capacity and cycling stability of NMC811/Li half cells *via* the formation of effective cathode electrolyte interphase (CEI) films.[213] However, compared with LiBOB, the CEI film formed from LiODFB is much thinner, more uniform and denser and contains more inorganic substances.[213] Placke *et al.* evaluated triphenylphosphine oxide (TPPO) as an additive for graphite/NMC811 lithium ion cells, which significantly enhanced the overall cell performance, leading to a higher discharge capacity and an increased initial coulombic efficiency (CE) as well as a high capacity retention of 80% after 295 cycles.[214] In addition, compared with other additives such as VC, triphenylphosphine (TPP) and diphenyl carbonate (DPC), the TPPO-containing electrolyte showed the highest discharge capacity and initial CE, as well as capacity retention after 100 cycles.[214] Lu *et al.* showed that 0.5 wt% adiponitrile (ADN) as an additive in a graphite/NMC811 Li-ion cell resulted in 17.6% higher capacity retention than that without the additive due to the formation of a dense coating layer on the NMC cathode *via* polymerization of ADN.[215]

It is often observed that a single additive improving the specific properties of the battery may have an adverse influence

on other properties, and therefore, a combination of additives is needed. For example, a thicker and more resistive CEI formed from LiBOB as an additive can be improved by using triphenylamine (Ph_3N) or 1,4-benzodiozane-6,7-diol (BDOD) as a co-additive, which can protect the positive electrode surface by forming an electronically conducting polymer through electrochemically initiated radical polymerization processes, reducing electrolyte oxidation and forming thinner CEI layers.[216] Dahn *et al.* systematically investigated electrolyte additives such as VC, fluoroethylene carbonate (FEC), methyl acetate (MA), 1,3,2-dioxathiolane-2,2-dioxide (DTD), LiBOB, lithium difluorophosphate (LFO), and their combinations on the cycling performance of single crystal (SC) and bimodal (BM) NMC811/graphite pouch cells.[208] They found that the cell with 2 wt% VC and 1 wt% DTD (2VC + 1DTD) had the best performance in long-term cycling at 40 °C and 55 °C, ultra-high precision charger (UHPC) cycling, and 60 °C storage, but it had high charge transfer resistance (R_{ct}) and ΔR_{ct}, which led to relatively poor performance in 20 °C and 1C long-term cycling. Although the cell with 2 wt% FEC and 1 wt% LFO (2FEC + 1 LFO) had lower R_{ct} and ΔR_{ct} than that with 2VC + 1DTD in cycling and storage tests, but it had poor capacity retention during cycling at 40 °C and 55 °C.[208] Winter *et al.* used 2 wt% 3-methyl-1,4,2-dioxazol-5-one (MDO) as an additive to a pure 1.0 M $LiPF_6$ in PC electrolyte, which could successfully cycle the NMC532/graphite full cell for more than 450 cycles with a remarkable capacity retention of 80%, whereas other additives such as VC and FEC failed.[217] Inspired by the effectiveness of MDO, Dahn *et al.* further investigated 3-phenyl-1,4,2-dioxazol-5-one (PDO) and its combination with other additives such as VC, DTD and LFO as additives in NMC622/graphite and NMC811/graphite pouch cells.[218] Although the cell with 2 wt% PDO and 1 wt% LFO (2PDO + 1% LFO) exhibited the best long term cycling stability of NMC811 cells, it still underperformed the reference cell in UHPC cycling and high-temperature storage. Interestingly, they found that 95% pure PDO was more promising than 99.8% pure PDO in the best-performing blend (2%PDO + 1% DTD) for long-term cycling and that (2% PDO + 2% VC) for high temperature storage.[218] The molecular structures of a few of the widely used electrolyte additives for NCM811 are shown in Fig. 17.

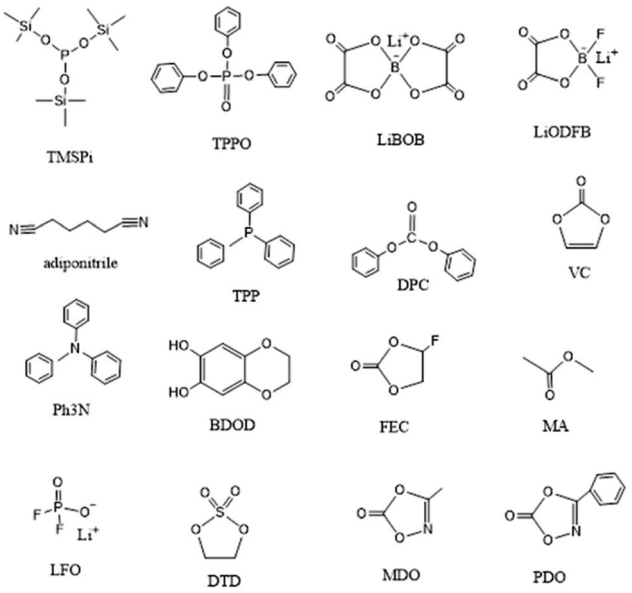

Fig. 17 Electrolyte additives for NCM811.

6 Selection of a suitable modification strategy

The challenges of Ni-rich NCM-based cathodes and the corresponding remedies are summarized in Table 1. It is observed that, a few of the issues, like cation mixing, poor Li^+ kinetics in the bulk, electronic conductivity, lattice oxygen escape, *etc.*, are required to be dealt with by electronic level modification. Cation/anion doping and single crystal structures are promising in these cases. On the other hand, the microcrack formation, surface reactivity with the electrolyte, *etc.*, can be mitigated by those strategies, which will protect the NCM-core from the direct contact of the electrolyte by modifying the cathode–electrolyte interface. Surface coating, core–shell or concentration gradient structures, electrolyte additives, *etc.*, are helpful in these cases. It is worth mentioning that high specific capacity with long term cycling performance of Ni-rich cathodes is critically required for high energy and power applications of LIBs, which can only be achieved by simultaneously resolving the electronic and surface level challenges. Although surface coating and ionic doping are efficient strategies, their benefits are limited. Considering the vastness of benefits, concentration gradient and single crystal modifications can be considered as the most efficient strategies to deal with the issues of Ni-rich cathodes. In the case of concentration gradient structures, the Ni-rich core offers high energy density, whereas the Mn and Co-rich shell is beneficial for providing structural/thermal stability, mitigating the side reaction and microcrack formation related issues, and thus ensures good capacity and long cycling performance of the Ni-rich cathode. On the other hand, a single crystal structure is promising to resolve both the electronic and surface-related issues. It helps to mitigate the issues, like phase transition caused by lattice oxygen escape, microcrack formation at the surface and propagation towards the bulk, and parasitic side reactions, and provides thermal/mechanical stability. However, industrial scale production of both the concentration gradient and single crystal structures with high phase purity is still in progress.

7 Ni-rich NCMs for solid-state LIBs

Solid-state batteries (SSBs), consisting of non-flammable inorganic solid electrolytes, are drawing considerable attention due to their high safety and improved energy density.[219] Similar to liquid electrolyte-based lithium-ion batteries, Ni-rich NCMs are also proved to be promising as high energy cathodes for SSBs. However, a decreased contact area, crystallographic imparity and high reactivity of solid electrolytes (SEs) with cathode active

Table 1 Issues and modification strategies of Ni-rich cathodes

Issues	Strategies
Li^+/Ni^{2+} mixing	➢Doping ➢Lower lithiation temperature
Slow Li^+ diffusion kinetics	➢Cation doping (pillar effect) ➢Conducting coating
Lattice oxygen release and phase transition	➢Doping ➢Interface engineering ➢Single crystal structure
Poor conductivity	➢Doping ➢Conductive coating
Thermal and mechanical stability	➢Core–shell structure ➢Concentration gradient structure ➢Single crystal
Cathode dissolution	➢Dual doping and coating ➢Core–shell structure ➢Concentration gradient structure
Microcrack	➢Coating ➢Core–shell structure ➢Concentration gradient structure ➢Electrolyte additive ➢Single crystal
Side reactions with the electrolyte	➢Coating ➢Core–shell structure ➢Concentration gradient structure ➢Electrolyte additive ➢Single crystal

materials (CAMs) at high voltage, *etc.*, are a few of the primary challenges to use Ni-rich NCMs as the cathode of SSBs.[220,221] The crystallographic mismatch of SEs and CAMs adversely affects the Li^+ diffusion through the interfaces. It is already discussed in the previous section that Ni-rich NCMs undergo volume shrinkage during the delithiation process, which creates severe stress problems at the interface of rigid SEs.[221] Among the various SEs, the garnet-type structure offers high Li^+ conductivity and widely used in the fabrication of solid-state LIBs. One common issue for garnet-based SSBs is that the incompatibility of NCMs with the solid electrolyte $Li_{6.45}Al_{0.05}La_3Zr_{1.6}Ta_{0.4}O_{12}$ (LLZO : Ta) causes the formation of highly resistive interphases during the co-sintering process. Roitzheim *et al.* have performed a detailed study on secondary phase formation during the co-sintering of NCM111/NCM811 and LLZO : Ta electrolytes with and without B-doping.[222] It was found that the interchange between Zr and Mn is more favorable compared to the interchange with Ni and Co as well as La ↔ Ni and La ↔ Co. It leads to the formation of a La-based, Mn-rich secondary phase of $LaCo_{1-3}$, which is predominant in NCM111. However, due to the presence of a smaller amount of Mn, a similar phase was not observed in NCM811. NCM811 mostly contains $La_2(Ni_{0.5}Li_{0.5})O_4$ as the secondary phase. The particle size and mass fraction of CAMs also have a significant role in achieving promising electrochemical performance of SSBs.[220,223] Jiang *et al.* have well depicted the competitive nature of the electronic and ionic conductivity through Fig. 18a.[220] Ni-rich NCMs with a small particle size demand a higher mass fraction of solid electrolytes to achieve facile ionic diffusion, whereas with the increase of particle size the CAM wt% is required to be increased to obtain effective electronic transportation. Several efforts have been made to improve the structural compatibility and electrochemical performance of Ni-rich NCM based solid state batteries. Recently, a hybrid electrolyte of the $Li_{6.4}La_3Zr_2Al_{0.2}O_{12}$ (LLZO) framework and poly(ε-caprolactone)-based solid polymer was utilized to fabricate a NCM811-cathode-based SSB.[224] Here, the LLZO provides an undisrupted ion-conduction pathway and poly(ε-caprolactone) offers flexibility and good interfacial adhesion with electrodes. It was observed that the NCM811 (with full concentration gradient or FCG)-based SSB shows better cycling performance compared to the conventional one. Improved structural robustness of FCG-NCM811 ensures a longer cycle life. Interfacial engineering is one of the promising strategies to improve the SSB performance. In order to improve the interfacial contact, Zhao *et al.* have constructed a hybrid layer of Li_3PO_4 and $Li_{6.4}La_3Zr_{1.4}Ta_{0.6}O_{12}$ (LLTZO) on NCM811.[225] This is achieved by an *in situ* calcination process, where the $NH_4H_2PO_4$-soaked $Ni_{0.8}Co_{0.1}Mn_{0.1}(OH)_2$ precursor was mixed with LiOH and $Li_{6.4}La_3Zr_{1.4}Ta_{0.6}O_{12}$ and calcined at 750 °C for 12 h under an oxygen atmosphere. From the surface energy calculation, it was observed that the surface energy follows the trend of NCM811(003) (0.89 J m^{-2}) < Li_3PO_4(002) (1.76 J m^{-2}) < $LLZTO_{(611)}$ (2.74 J m^{-2}) (Fig. 18b).[225] Li_3PO_4 with an intermediate surface energy acts as the bridge between the NCM811 and LLZTO layers and facilitates the Li^+ transfer from the cathode surface to the electrolyte. The binder like Li_3PO_4 not only disintegrates the space charge across the interface, but also increases the density of the LLZTO electrolyte and improves the conductivity. The NCM811-LP-LLZTO SSB shows good electrochemical performance at various temperatures of 30, 55 and 80 °C. However, the capacity retention was observed to decrease with the increase of operating temperatures. Various modified polymer electrolytes, such as g-C_3N_4 nanosheet (GCN) reinforced poly(vinylidene fluoride) (PVDF-GCN), poly(vinylidene-cotrifluoroethylene) [P(VDF-TrFE)], decabromodiphenyl ethane (DBDPE) added poly(ethylene oxide) (PEO), trifluoroethyl methacrylate (TFEMA)–PEO, *etc.*, offer stable solid-electrolyte interfaces and improve the NCM811-based SSB performance.[226–229] Li *et al.* have synthesized trifluoroethyl methacrylate (PTFEMA)–PEO by electropolymerization.[229] The PTFEMA layer modified the NCM811-electrolyte interface and plays the following roles: (i) offers undisrupted transport of Li^+ across the interface, (ii) mitigates the electrolyte oxidation at high voltage, (iii) prevents the microcrack formation and (iv) buffers the stress, generated by volume change in NCM811 particles during charge–discharge cycling.

As mentioned in the previous sections, the anisotropic volumetric strain during the discharge process is more prominent in the case of densely packed polycrystalline NCMs, composed of randomly distributed grains. In this aspect, single crystal Ni-rich NCMs, composed of orderly packed primary particles, have a high prospect as a high performance cathode for SSBs.[221,230–232] Li *et al.* have utilized $LiNbO_3$-coated single

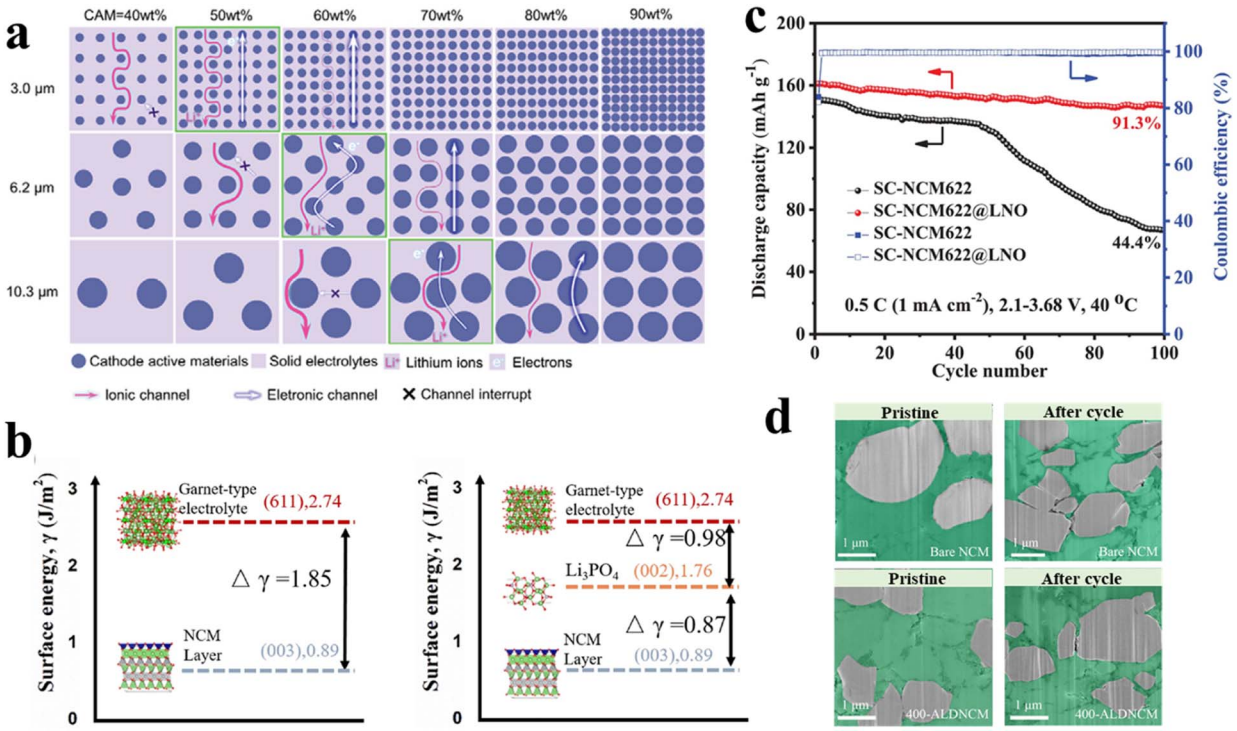

Fig. 18 (a) Schematic illustration demonstrating the inter-dependence between the particle size, wt% of CAM with electronic and ionic conductivity in SSBs (adapted with permission.[220] Copyright 2022, Wiley-VCH.), (b) surface energy profiles of NCM811 and solid-electrolytes with and without interface engineered with Li_3PO_4 (adapted with permission.[225] Copyright 2021, Elsevier.), (c) profile showing the cycling performance of a single crystal NCM622 based SSB with and without $LiNbO_3$ coating (adapted with permission.[230] Copyright 2020, Elsevier.) and (d) cross-sectional SEM images of pristine and atomic layer deposited/LNO coated-NCM811 electrodes before and after cycling (adapted with permission.[231] Copyright 2021, American Chemical Society).

crystal NCM622 as the cathode to fabricate a $Li_{9.54}Si_{1.74}P_{1.44}S_{11.7}Cl_{0.3}$ (LSPSC)-SE based SSB.[230] Single crystal NCM622 was synthesized by mixing a coprecipitation derived $Ni_{0.6}Co_{0.2}Mn_{0.2}(OH)_2$ precursor with Li_2CO_3 followed by high temperature calcination at 1000 °C for 10 h in a muffle furnace. The final micron-sized SC-NCM622 was obtained by further calcining the oxide with a stoichiometric amount of Li_2CO_3 at 900 °C for 12 h. In the first step Li_2CO_3 plays the role of a molten salt and in the second step it acts as the Li source. $LiNbO_3$-coated SC-NCM622 was synthesized by treating SC-NCM622 in an ethanolic solution of $Nb(C_2H_5O)_5$ followed by calcination at 400 °C for 1 h under an oxygen flow. The as-fabricated SSB shows a high specific capacity of 177.9 mA h g^{-1} at 0.1C (0.2 mA cm^{-2}) and a capacity retention of 91.3% after 100 cycles at 0.5C (Fig. 18c).[230] The coating and single crystal structure of the cathode jointly plays an important role in protecting the surface from side reactions and preventing microcrack formation. Liu *et al.* have coated SC-NCM811 with a nano-lithium niobium oxide (LNO) layer by a modified atomic layer deposition method.[231] The as-fabricated cathode and $Li_{10}SnP_2S_{12}$ (LSPS)-SE based SSB achieves a high specific capacity of 205 mA h g^{-1} at 0.1C and retained up to 116 mA h g^{-1} at 1C. The nano-LNO layer plays the dual role of mitigating the solid electrolyte decomposition and stabilizes the cathode/SE interface. From the cross-sectional SEM images, it is observed that the single crystal structure both with coating and without coating shows good structural stability before and after cycling and microstructural disintegration is not an issue for them (Fig. 18d).[231] Further studies reveal that the efficient surface modification of single crystal Ni-rich NCMs can prevent the unwanted phase transition and improve the cycling performance of SSBs.[232]

8 Summary and outlook

The gradual shift of the world economy towards low/zero-carbon emission demands the increasing manufacturing of cost-efficient and environmentally benign EVs, which further urges the accelerated production of LIBs with high energy density and long cycle life. The electrochemical performance and cost of LIBs crucially depend on the economical production of each component, such as the cathode, anode, electrolyte, and separator. Among them, the selection and synthesis of an efficient cathode material is the key step to achieve high specific capacity, good rate capability, and long cycling stability of LIBs. Although NCM111 is already commercialized for EV production, it suffers from high cost and socio-political issues related to the higher cobalt-content. This motivates various state governments and the transport industry to search for low-cobalt-based cathode materials. As cobalt plays a crucial role in mitigating Li^+/Ni^{2+} mixing in lithiated nickel-cobalt-manganese-based layered oxide (NCM) moieties, complete removal of cobalt from the material is a tedious task and

rational design is required to produce cobalt-less/free cathode materials with good cycling and rate performance. Nickel offers high energy density and manganese is responsible for the high thermal and mechanical stability of the NCM structure. The search for cobalt-free/less cathodes unfolded a number of parallel research directions in the field of LIB cathode material design. The following are the various cobalt-free cathodes developed so far: Co-free lithium rich cathodes,[233–237] Co-free nickel rich cathodes,[238–240] spinel cathodes,[241–243] olivine,[10,244] *etc.* Low-cobalt and high nickel content NCMs also have enormous commercial prospects as the cathodes of high performance EV batteries. Various aspects of Ni-rich NCMs, including synthesis, issues and probable remedies, are critically reviewed in this article.

The superiority of any of the synthesis methods is determined by the following points: (i) production rate, (ii) manufacturing cost, (iii) quality of the cathode material (in terms of the morphology, particle size distribution, tap density, cation mixing, *etc.*) and (iv) human labor involved. Most of those synthetic routes, except solid-state synthesis, generally produce NCM-precursors as the product, which are further required to be lithiated at high temperature and under a high oxygen flow to obtain the final layered oxide-based cathode material. Although the solid-state process is widely utilized in commercial scale synthesis of NCM111, there are few reports on the solid-state production of high Ni-content NCMs, due to the lack of homogeneity and poor control over the composition. On the other hand, the production of a cathode material in bulk is challenging for sol–gel and solvothermal synthesis. Spray-pyrolysis is proved to be an efficient synthesis process for Ni-rich cathode materials with a uniform particle size and morphology. However, the tap density of the particles is not satisfactory. Among the other routes, the co-precipitation process is superior by the virtues of cost-effectiveness, homogeneous mixing of the salts and control over the particle size and morphology of the precursors and hence extensively utilized to produce NCMs with various compositions. The three types of co-precipitation reactions, including hydroxide, carbonate and oxalate methods, are described in this review with their intrinsic advantages and disadvantages. Although the production rate of the traditional co-precipitation batch process is higher than that of other processes, it solely depends on the size of the stirred-tank reactor and the composition varies for each batch synthesis. The upgraded and more controllable version of the batch process involves semi-batch reactors with open inlets and/or outlets, where the chemicals are fed into the temperature-controlled flask continuously. However, similar to the batch in the case of a semi-batch setup, the yield of the product depends on the size of the reactor. Besides this, a significant variation in the microenvironments in terms of temperature, pH and concentration is also observed in the different parts of the reaction vessel, which further affects the uniformity of the particle nature. To get rid of all those issues and to improve the production rate of the co-precipitation process, a continuous manufacturing platform is needed at this hour. We have proposed a three-phasic slug-flow-based continuous synthesis platform for the production of NCM-based cathode materials of tunable composition. In this case, the co-precipitation reaction takes place inside each of the micro-liter slugs formed inside the tubular reactor with a similar micro-environment and hence the production rate can be changed only by changing the feeding volume of the reactants without affecting the quality of the product. A more efficient continuous manufacturing platform is required to be developed to make high performance EV batteries economically viable and customer friendly. The lithiation step is also crucial to determine the final product quality. Proper optimization in terms of the heating rate, highest calcination temperature, flow-rate of oxygen, *etc.*, are the important parameters to achieve Ni-rich NCMs with a uniform morphology and high crystallinity and tap density. The homogeneous mixing of a lithium salt with NCM precursors (hydroxide/oxalate/carbonate) has great importance to achieve higher capacity and good rate performance. Hence, it is better to mix the lithium salt with the transition metal salt solution at the beginning of the precursor synthesis to produce Li-embedded NCM precursors. However, this is delicate work and optimization of appropriate reaction conditions is needed.

Ni-rich NCMs suffer from various issues, such as cation mixing, microcrack formation, poor thermal and high voltage stability. The cation mixing is caused due the following three reasons: (i) similar size of Ni^{2+} and Li^{+}, (ii) strong interplanar superexchange interaction of Ni^{2+}–O–Ni^{2+} and (iii) low migration barrier of Ni^{2+} in the NCM structure. The high extent of Ni^{2+}/Li^{+} mixing deteriorates the rate performance and makes the Li^{+} diffusion kinetics sluggish. Although the higher cut-off voltage improves the specific capacity of the Ni-rich cathode, the side reactions caused due to high voltage charging have severe adverse effects on the electrochemical performance and stability of the cathode. The issues arise due to the high voltage charging, such as the formation of oxygen vacancies, TM dissolution, irreversible phase change of the cathode, *etc.* High temperature also affects the stability of Ni-rich NCMs. The deposition of metals on the cathode, short circuiting, and volume expansion of the cell due to various gas evolution are a few of the major issues caused due to the high temperature. On the other hand, the cracking of secondary particles of Ni-rich NCMs is primarily caused by the continuous volume change of the NCM crystals due to insertion/extraction of Li^{+} upon charge and discharge. The microcrack formation largely depends on the depth of discharge (DOD). Once the microcrack forms on the surface, exposed to the electrolyte, it propagates towards the bulk and causes severe damage in the cathode particle. The H2 to H3 phase change of Ni-rich NCMs at a voltage of >4.2 V *vs.* Li/Li^{+} is also one of the reasons behind cracking-related issues. The microcrack formation severely hampers the cycle life of the Ni-rich cathode and hence this is a burning issue on the way of commercialization. The phase change caused by the lattice oxygen escape is also responsible for the poor cycling performance of Ni-rich NCMs.

In order to mitigate the issues related to high Ni-content NCMs, several modification strategies, including (i) functional coating, (ii) cation/anion doping, (iii) core–shell structures, (iv) gradient structures, (v) single crystals, *etc.*, have been exploited

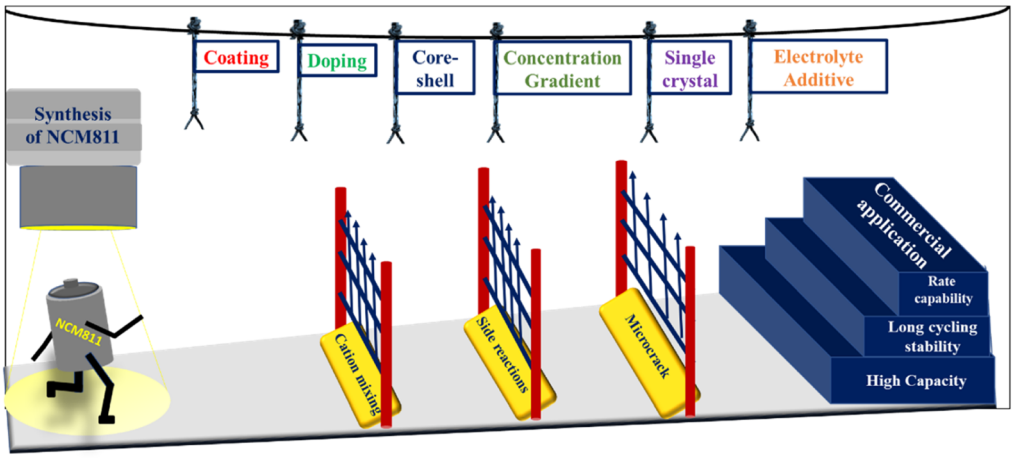

Fig. 19 Schematic representation of the issues and modification strategies related to the NCM811-based LIB cathode material.

to date. Coating with oxides, phosphides and fluorides, conducting polymers, Li-containing inorganic materials and ionic liquids is found to be beneficial in protecting the NCM surface from direct exposure to the electrolyte and prevent not only side reactions but also stop micro-crack formation. Thus, it improves the cycling stability of Ni-rich NCMs. The primary criteria for a suitable coating material are that it should be (a) electrochemically inactive within the active voltage window of the cathode, (b) inert towards the electrolyte, (c) provide sufficient channels for Li^+ diffusion throughout the cathode, (d) cost-effective and last but not the least (e) environmentally friendly. The Li^+ diffusion kinetics varies with the thickness of the coating layer. However, achieving a uniform coating layer is a delicate task and efficient handling is crucially required. The doping of cations/anions into the crystal moiety of NCM offers improved conductivity as well as decreased cation mixing and metal dissolution from the cathode, which further improves the rate capability and active voltage window of the Ni-rich cathode. However, excess doping may cause sluggish Li^+ diffusion. Hence the optimization of the doping parameters and proper control over the process are needed. Instead of one, dual modification with doping and coating synergistically improves the overall electrochemical performance of Ni-rich cathodes. Substantial research progress in the direction of cost-efficient dual modification techniques is highly required. Core-shell synthesis has the benefits similar to chemical coating. A manganese-rich shell provides sufficient mechanical strength to the material. The major limitation of this structure is the difference between the core and shell crystal parameters leading to an unequal volume change and deteriorates the cycling performance. The issue related to abrupt change in composition in the case of the core–shell structure is solved by the strategy of producing Ni-rich NCMs with concentration gradient. In this case, the concentration of Ni gradually decreases from the center towards the edge and the Mn concentration follows the opposite direction to form a Ni-rich core with a Mn-rich shell but with gradual change in composition as well as the lattice parameters. Co-precipitation chemistry is generally utilized to produce NCM precursors with concentration gradient, which is hard to maintain after the high temperature lithiation step. The gradient becomes smoother due to the thermal diffusion of the transition metals. A few of the recent groups have demonstrated that doping may help to retain the gradient feature in the oxide state, which still requires extensive analysis to draw a firm conclusion. Besides this, although this strategy is proven to be efficient in terms of electrochemical performance, producing a NCM with full concentration gradient through a continuous reactor is tricky. Efficient design of a continuous reactor with multiple metal salt-feeding points to produce Ni-rich NCMs with concentration gradient could be an important sector of battery research. The synthesis of single-crystal NCMs is also an efficient way to achieve long cycling stability without particle cracking. Proper synthetic design to produce single crystal NCMs in bulk without losing the phase purity is also one of the future scopes of battery research. Improvement in cathode performance also can be achieved by using single or multiple electrolyte additives, which will protect the cathode surface by forming a passivation layer and ensures longer cycling performance. However, the presence of an excess additive may adversely affect the viscosity and conductivity of the electrolyte. Hence, proper optimization and control over the additive amount are crucially required to get the benefit. The performance of NCM811 after applying various modification strategies by several research groups is enlisted as the tabular form in Table S1.†

Ni-rich NCMs, specifically NCM811, have a great prospect to achieve industrial success as an EV battery cathode. The synthesis of efficient Ni-rich NCMs as well as solid electrolytes for high performance solid-state batteries is one of the primary targets in the field of LIB technology. The commercial success of Ni-rich NCMs is only possible by developing an efficient manufacturing platform to produce commercial scale and impurity-free materials as well as cost-effective performance improving modification technologies (Fig. 19).

Author contributions

S. M. collected the literature and wrote the original draft of the manuscript. A. P. and J. M contributed to the reviewing, reference and figure management. X. G. S. and M. P. P wrote the "electrolyte additive" section and reviewed the manuscript. M. J. and M. M. developed and wrote the "slug-flow manufacturing" part. M. L. R. contributed to the mathematical modelling part of the co-precipitation synthesis. H. L. helped with the experimental design of the scaling up process. R. B. G. and M. J. conceived the idea and supervised the project. All of the authors contributed to the writing and reviewing of the manuscript and approved the final version of the manuscript.

Conflicts of interest

The authors declare no conflict of interest.

Acknowledgements

This material is based upon work supported by Virginia Commonwealth University, National Science Foundation under Grant No. CMMI-1940948 and government support under contract number DE-EE0009110 awarded by the Advanced Manufacturing Office (AMO) of the Office of Energy Efficiency and Renewable Energy (EERE) under the US department of energy. The government has certain rights in the work. This manuscript has been authored by UT-Battelle, LLC under Contract No. DEAC05-00OR22725 with the U.S. Department of Energy. The United States Government retains and the publisher, by accepting the article for publication, acknowledges that the United States Government retains a non-exclusive, paid-up, irrevocable, worldwide license to publish or reproduce the published form of this manuscript, or allow others to do so, for United States Government purposes. The Department of Energy will provide public access to these results of federally sponsored research in accordance with the DOE Public Access Plan (**http://energy.gov/downloads/doe-public-access-plan**).

References

1 **https://www.un.org/development/desa/disabilities/envision2030.html/**, accessed: 25th March, 2022.
2 United Nations, *Paris Declaration on Electro-Mobility and Climate Change & Call to Action*, **https://unfccc.int/news/the-paris-declaration-on-electro-mobility-and-climate-change-and-call-to-action**, accessed: 25th March, 2022.
3 C. McKerracher, *et al.*, in *Electric Vehicle Outlook 2020*, Bloomberg New Energy Finance, 2021.
4 **https://theicct.org/publication/a-global-comparison-of-the-life-cycle-greenhouse-gas-emissions-of-combustion-engine-and-electric-passenger-cars/**, accessed on 13th Sep, 2022.
5 **https://www.statista.com/chart/25412/life-cycle-emissions-savings-of-electric-cars/**, accessed on 13th Sep, 2022.
6 Statistic_id1011187_global-lithium-ion-battery-market-2020-2026.
7 K. Mizushima, P. C. Jones, P. J. Wiseman and J. B. Goodenough, *Mater. Res. Bull.*, 1980, **15**, 783–789.
8 N. Muralidharan, E. C. Self, M. Dixit, Z. Du, R. Essehli, R. Amin, J. Nanda and I. Belharouak, *Adv. Energy Mater.*, 2022, **12**, 2103050.
9 *"State of the Cobalt Market" Report*, Cobalt institute, May 2021.
10 H. Zhao, W. Y. A. Lam, L. Sheng, L. Wang, P. Bai, Y. Yang, D. Ren, H. Xu and X. He, *Adv. Energy Mater.*, 2022, **12**, 2103894.
11 B. E. Murdock, K. E. Toghill and N. Tapia-Ruiz, *Adv. Energy Mater.*, 2021, **11**, 2102028.
12 *Tesla*, **https://www.tesla.com**.
13 M. Wentker, M. Greenwood and J. Leker, *Energies*, 2019, **12**, 504.
14 H. Dong and G. M. Koenig, *CrystEngComm*, 2020, **22**, 1514–1530.
15 L. Noerochim, S. Suwarno, N. H. Idris and H. K. Dipojono, *Batteries*, 2021, **7**, 84.
16 M. Akhilash, P. S. Salini, B. John and T. D. Mercy, *J. Alloys Compd.*, 2021, **869**, 159239.
17 K. H. Choi, X. Liu, X. Ding and Q. Li, *Ionics*, 2020, **26**, 1063–1080.
18 S. Hy, H. Liu, M. Zhang, D. Qian, B. J. Hwang and Y. S. Meng, *Energy Environ. Sci.*, 2016, **9**, 1931–1954.
19 Y. Shen, Y. Wu, H. Xue, S. Wang, D. Yin, L. Wang and Y. Cheng, *ACS Appl. Mater. Interfaces*, 2021, **13**, 717–726.
20 Y. Kim, W. M. Seong and A. Manthiram, *Energy Storage Mater.*, 2021, **34**, 250–259.
21 W. Li, B. Song and A. Manthiram, *Chem. Soc. Rev.*, 2017, **46**, 3006–3059.
22 F. T. Geldasa, M. A. Kebede, M. W. Shura and F. G. Hone, *RSC Adv.*, 2022, **12**, 5891–5909.
23 M. Mou, A. Patel, S. Mallick, J. Mugumya, M. L. Rasche, M. Parans Paranthaman, H. Lopez, G. P. Pandey, R. B. Gupta and M. Jiang, *ACS Omega*, 2022, **7**(46), 42408–42417.
24 M. Mou, A. Patel, S. Mallick, K. Jayanthi, X.-G. Sun, M. P. Paranthaman, S. Kothe, E. Baral, S. Saleh, J. H. Mugumya, Mi. L. Rasche, R. B. Gupta, H. Lopez, and M. Jiang, 2022. (submitted).
25 J. H. Mugumya, M. L. Rasche, R. F. Rafferty, A. Patel, S. Mallick, M. Mou, J. A. Bobb, R. B. Gupta and M. Jiang, *Energy Fuels*, 2022, **36**, 12261–12270.
26 Y. Shen, H. Xue, S. Wang, Z. Wang, D. Zhang, D. Yin, L. Wang and Y. Cheng, *J. Colloid Interface Sci.*, 2021, **597**, 334–344.
27 M. Amou, B. Larhrib and I. Saadoune, *J. Electroanal. Chem.*, 2021, **881**, 114957.
28 A. Gomez-Martin, F. Reissig, L. Frankenstein, M. Heidbüchel, M. Winter, T. Placke and R. Schmuch, *Adv. Energy Mater.*, 2022, **12**, 2103045.
29 Z. Zhao, B. Zhang, J. Zou, P. Li, Z. Liu, L. Cheng, X. Ou and J. Zhang, *J. Energy Storage*, 2022, **45**, 103512.
30 B. Zhang, L. Cheng, P. Deng, Z. Xiao, L. Ming, Y. Zhao, B. Xu, J. Zhang, B. Wu and X. Ou, *J. Alloys Compd.*, 2021, **872**, 159619.

31 G. Zha, W. Hu, S. Agarwal, C. Ouyang, N. Hu and H. Hou, *Chem. Eng. J.*, 2021, **409**, 128343.
32 H. H. Sun and A. Manthiram, *Chem. Mater.*, 2017, **29**, 8486–8493.
33 J. Hu, L. Li, E. Hu, S. Chae, H. Jia, T. Liu, B. Wu, Y. Bi, K. Amine, C. Wang, J. Zhang, J. Tao and J. Xiao, *Nano Energy*, 2021, **79**, 105420.
34 J. Zheng, P. Yan, L. Estevez, C. Wang and J. G. Zhang, *Nano Energy*, 2018, **49**, 538–548.
35 L. Liang, K. Du, Z. Peng, Y. Cao, J. Duan, J. Jiang and G. Hu, *Electrochim. Acta*, 2014, **130**, 82–89.
36 Y. Shen, X. Yao, J. Zhang, S. Wang, D. Zhang, D. Yin, L. Wang, Y. Zhang, J. Hu, Y. Cheng and X. Li, *Nano Energy*, 2022, **94**, 106900.
37 A. L. Lipson, B. J. Ross, J. L. Durham, D. Liu, M. Leresche, T. T. Fister, L. Liu and K. Kim, *ACS Appl. Energy Mater.*, 2021, **4**, 1972–1977.
38 C. Roitzheim, L. Y. Kuo, Y. J. Sohn, M. Finsterbusch, S. Möller, D. Sebold, H. Valencia, M. Meledina, J. Mayer, U. Breuer, P. Kaghazchi, O. Guillon and D. Fattakhova-Rohlfing, *ACS Appl. Energy Mater.*, 2022, **5**, 524–538.
39 C. S. Yoon, H. H. Ryu, G. T. Park, J. H. Kim, K. H. Kim and Y. K. Sun, *J. Mater. Chem. A*, 2018, **6**, 4126–4132.
40 R. Lin, S. M. Bak, Y. Shin, R. Zhang, C. Wang, K. Kisslinger, M. Ge, X. Huang, Z. Shadike, A. Pattammattel, H. Yan, Y. Chu, J. Wu, W. Yang, M. S. Whittingham, H. L. Xin and X. Q. Yang, *Nat. Commun.*, 2021, **12**, 2350.
41 Y. Ding, D. Mu, B. Wu, Z. Zhao and R. Wang, *Ceram. Int.*, 2020, **46**, 9436–9445.
42 G. Zang, J. Zhang, S. Xu and Y. Xing, *Energy*, 2021, **218**, 119504.
43 C. Ma, M. Chen, Z. Ding, B. Wei, C. Liang, L. Zhou, L. Chen, X. Ji, P. Gao and W. Wei, *Nano Energy*, 2022, **93**, 106803.
44 Z. Li, B. Guo, Y. Chen, J. Chen, Z. Ma, X. Liu, J. Yang, Y. Chen, Y. Huang, M. Wang and X. Li, *J. Power Sources*, 2021, **487**, 229410.
45 V. Pimenta, M. Sathiya, D. Batuk, A. M. Abakumov, D. Giaume, S. Cassaignon, D. Larcher and J. M. Tarascon, *Chem. Mater.*, 2017, **29**, 9923–9936.
46 F. Guo, Y. Xie and Y. Zhang, *Nano Res.*, 2022, **15**, 2052–2059.
47 X. Yao, Z. Xu, Z. Yao, W. Cheng, H. Gao, Q. Zhao, J. Li and A. Zhou, *Mater. Today Commun.*, 2019, **19**, 262–270.
48 L. Tang, X. Cheng, R. Wu, T. Cao, J. Lu, Y. Zhang and Z. Zhang, *J. Energy Chem.*, 2022, **66**, 9–15.
49 A. S. Myerson, *Handbook of Industrial Crystallization*, Butterworth-Heinemann, Woburn, MA, 2nd edn, 2002.
50 M. Abolhasani, C. W. Coley, L. Xie, O. Chen, M. G. Bawendi and K. F. Jensen, *Chem. Mater.*, 2015, **2**, 6131–6138.
51 M. Mou and M. Jiang, *J. Pharm. Innovation*, 2020, **15**, 281–294.
52 S. Wang, M. Jiang, S. Ibrahim, J. Wu, X. Feng, X. Duan, Z. Yang, C. Yang and N. Ohmura, *Chem. Eng. Technol.*, 2016, **39**, 680–688.
53 M. Jiang, Z. Zhu, E. Jimenez, C. D. Papageorgiou, J. Waetzig, A. Hardy, M. Langston and R. D. Braatz, *Cryst. Growth Des.*, 2014, **14**, 851–860.
54 M. Mou, H. Li, B. Yang and M. Jiang, *Crystals*, 2019, **9**, 412.
55 M. Abolhasani, C. W. Coley, L. Xie, O. Chen, M. G. Bawendi and K. F. Jensen, *Chem. Mater.*, 2015, **27**, 6131–6138.
56 M. Jiang and R. D. Braatz, *Chem. Eng. Technol.*, 2018, **41**, 143–148.
57 L. Zhu, C. Bao, L. Xie, X. Yang and X. Cao, *J. Alloys Compd.*, 2020, **831**, 154864.
58 M. Zhang, C. Wang, J. Zhang, G. Li and L. Gu, *ACS Omega*, 2021, **6**, 16465–16471.
59 S. J. Shi, J. P. Tu, Y. Y. Tang, Y. X. Yu, Y. Q. Zhang, X. L. Wang and C. D. Gu, *J. Power Sources*, 2013, **228**, 14–23.
60 D. Jiang, L. Zhao, Y. Shao and D. Wang, *RSC Adv.*, 2015, **5**, 40779–40784.
61 H. Lu, H. Zhou, A. M. Svensson, A. Fossdal, E. Sheridan, S. Lu and F. Vullum-Bruer, *Solid State Ionics*, 2013, **249–250**, 105–111.
62 C. M. Subramaniyam, H. Celio, K. Shiva, H. Gao, J. B. Goodneough, H. K. Liu and S. X. Dou, *Sustainable Energy Fuels*, 2017, **1**, 1292–1298.
63 C. Zhang, J. Qi, H. Zhao, H. Hou, B. Deng, S. Tao, X. Su, Z. Wang, B. Qian and W. Chu, *Mater. Lett.*, 2017, **201**, 1–4.
64 Y. Zhang, K. Du, Y. Cao, Y. Lu, Z. Peng, J. Fan, L. Li, Z. Xue, H. Su and G. Hu, *J. Power Sources*, 2020, **477**, 228701.
65 M. Jiang, Q. Zhang, X. Wu, Z. Chen, D. L. Danilov, R. A. Eichel and P. H. L. Notten, *ACS Appl. Energy Mater.*, 2020, **3**, 6583–6590.
66 Y. Lu, Z. Gan, J. Xia, K. Du, Z. Peng, Y. Cao, G. Hu and J. Xiao, *ChemElectroChem*, 2019, **6**, 5661–5670.
67 M. Lengyel, G. Atlas, D. Elhassid, P. Y. Luo, X. Zhang, I. Belharouak and R. L. Axelbaum, *J. Power Sources*, 2014, **262**, 286–296.
68 J. Zhu, J. Zheng, G. Cao, Y. Li, Y. Zhou, S. Deng and C. Hai, *J. Power Sources*, 2020, **464**, 228207.
69 J. Zhang, V. L. Muldoon and S. Deng, *J. Power Sources*, 2022, **528**, 231244.
70 C. Abram, J. Shan, X. Yang, C. Yan, D. Steingart and Y. Ju, *ACS Appl. Energy Mater.*, 2019, **2**, 1319–1329.
71 M. Lengyel, D. Elhassid, G. Atlas, W. T. Moller and R. L. Axelbaum, *J. Power Sources*, 2014, **266**, 175–178.
72 B. L. Ellis, K. T. Lee and L. F. Nazar, *Chem. Mater.*, 2010, **22**, 691–714.
73 N. Y. Kim, T. Yim, J. H. Song, J. S. Yu and Z. Lee, *J. Power Sources*, 2016, **307**, 641–648.
74 D. Wang, C. Xin, M. Zhang, J. Bai, J. Zheng, R. Kou, J. Y. Peter Ko, A. Huq, G. Zhong, C. J. Sun, Y. Yang, Z. Chen, Y. Xiao, K. Amine, F. Pan and F. Wang, *Chem. Mater.*, 2019, **31**, 2731–2740.
75 J. Zheng, G. Teng, C. Xin, Z. Zhuo, J. Liu, Q. Li, Z. Hu, M. Xu, S. Yan, W. Yang and F. Pan, *J. Phys. Chem. Lett.*, 2017, **8**, 5537–5542.
76 J. Kanamori, *J. Phys. Chem. Solids*, 1959, **10**, 87–98.
77 J. B. Goodenough, *Magnetism and the Chemical Bond*, Interscience, New York, 1963.
78 Y. Xiao, T. Liu, J. Liu, L. He, J. Chen, J. Zhang, P. Luo, H. Lu, R. Wang, W. Zhu, Z. Hu, G. Teng, C. Xin, J. Zheng, T. Liang, F. Wang, Y. Chen, Q. Huang, F. Pan and H. Chen, *Nano Energy*, 2018, **49**, 77–85.

79 J. Zheng, Y. Ye, T. Liu, Y. Xiao, C. Wang, F. Wang and F. Pan, *Acc. Chem. Res.*, 2019, **52**, 2201–2209.
80 Y. Kim, D. Kim and S. Kang, *Chem. Mater.*, 2011, **23**, 5388–5397.
81 M. J. Zhang, G. Teng, Y. C. K. Chen-Wiegart, Y. Duan, J. Y. P. Ko, J. Zheng, J. Thieme, E. Dooryhee, Z. Chen, J. Bai, K. Amine, F. Pan and F. Wang, *J. Am. Chem. Soc.*, 2018, **140**, 12484–12492.
82 Y. Chen, Y. Li, W. Li, G. Cao, S. Tang, Q. Su, S. Deng and J. Guo, *Electrochim. Acta*, 2018, **281**, 48–59.
83 Z. Wu, C. Cao, X. Yan, X. Zang, Y. Zhao, X. Ma, R. Liu, L. Hu, Y. Jiang and S. Sun, *Electrochim. Acta*, 2019, **302**, 153–160.
84 S. W. Lee, M. S. Kim, J. H. Jeong, D. H. Kim, K. Y. Chung, K. C. Roh and K. B. Kim, *J. Power Sources*, 2017, **360**, 206–214.
85 S. Liu, J. Su, J. Zhao, X. Chen, C. Zhang, T. Huang, J. Wu and A. Yu, *J. Power Sources*, 2018, **393**, 92–98.
86 W. Li, X. Liu, Q. Xie, Y. You, M. Chi and A. Manthiram, *Chem. Mater.*, 2020, **32**, 7796–7804.
87 S. K. Jung, H. Gwon, J. Hong, K. Y. Park, D. H. Seo, H. Kim, J. Hyun, W. Yang and K. Kang, *Adv. Energy Mater.*, 2014, **4**, 1300787.
88 J. Kim, H. Ma, H. Cha, H. Lee, J. Sung, M. Seo, P. Oh, M. Park and J. Cho, *Energy Environ. Sci.*, 2018, **11**, 1449–1459.
89 Y. K. Ahn, Y. N. Jo, W. Cho, J. S. Yu and K. J. Kim, *Energies*, 2019, **12**, 1638.
90 J. Qian, L. Liu, J. Yang, S. Li, X. Wang, H. L. Zhuang and Y. Lu, *Nat. Commun.*, 2018, **9**, 4918.
91 C. Wu, Y. Wu, X. Feng, H. Wang, F. Zhang, S. Chen, B. Li, T. Deng and M. Ouyang, *J. Energy Storage*, 2022, **52**, 104870.
92 D. Wang, L. Zheng, X. Li, G. Du, Y. Feng, L. Jia and Z. Dai, *Int. J. Energy Res.*, 2020, **44**, 12158–12168.
93 H. Li, L. Chen and Z. Chen, *SN Appl. Sci.*, 2020, **2**, 1136.
94 Z. Feng, X. Huang, R. Rajagopalan, Y. Tang, Z. Peng and H. Wang, *J. Electrochem. Soc.*, 2019, **166**, A1439–A1448.
95 J. Li, Z. Zhou, Z. Luo, Z. He, J. Zheng, Y. Li, J. Mao and K. Dai, *Sustainable Mater. Technol.*, 2021, **29**, e00305.
96 K. Dokko, M. Nishizawa, S. Horikoshi, T. Itoh, M. Mohamedi and I. Uchida, *Electrochem. Solid-State Lett.*, 2000, **3**, 125–127.
97 K. J. Park, J. Y. Hwang, H. H. Ryu, F. Maglia, S. J. Kim, P. Lamp, C. S. Yoon and Y. K. Sun, *ACS Energy Lett.*, 2019, **4**, 1394–1400.
98 H. H. Ryu, K. J. Park, C. S. Yoon and Y. K. Sun, *Chem. Mater.*, 2018, **30**, 1155–1163.
99 L. Wang, A. Dai, W. Xu, S. Lee, W. Cha, R. Harder, T. Liu, Y. Ren, G. Yin, P. Zuo, J. Wang, J. Lu and J. Wang, *J. Am. Chem. Soc.*, 2020, **142**, 14966–14973.
100 Z. Xu, X. Guo, J. Z. Wang, Y. Yuan, Q. Sun, R. Tian, H. Yang and J. Lu, *Adv. Energy Mater.*, 2022, **12**, 2201323.
101 C. Liao, F. Li and J. Liu, *Nanomaterials*, 2022, **12**, 1888.
102 W. M. Dose, I. Temprano, J. P. Allen, E. Björklund, C. A. O'Keefe, W. Li, B. L. Mehdi, R. S. Weatherup, M. F. L. De Volder and C. P. Grey, *ACS Appl. Mater. Interfaces*, 2022, **14**, 13206–13222.
103 S. M. Bak, K.-W. Nam, W. Chang, X. Yu, E. Hu, S. Hwang, E. A. Stach, K. B. Kim, K. Y. Chung and X.-Q. Yang, *Chem. Mater.*, 2013, **25**, 337–351.
104 T. Wang, K. Ren, W. Xiao, W. Dong, H. Qiao, A. Duan, H. Pan, Y. Yang and H. Wang, *J. Phys. Chem. C*, 2020, **124**, 5600–5607.
105 R. Jung, M. Metzger, F. Maglia, C. Stinner and H. A. Gasteiger, *J. Electrochem. Soc.*, 2017, **164**, A1361–A1377.
106 S. Oswald, D. Pritzl, M. Wetjen and H. A. Gasteiger, *J. Electrochem. Soc.*, 2021, **168**, 120501.
107 K. Jia, J. Wang, J. Ma, Z. Liang, Z. Zhuang, G. Ji, R. Gao, Z. Piao, C. Li, G. Zhou and H.-M. Cheng, *Nano Lett.*, 2022, **22**, 8372–8380.
108 C. Zhang, B. Wei, W. Jiang, M. Wang, W. Hu, C. Liang, T. Wang, L. Chen, R. Zhang, P. Wang and W. Wei, *ACS Appl. Mater. Interfaces*, 2021, **13**, 45619–45629.
109 X. Ren, Y. Li, X. Xi, S. Liu, Y. Xiong, D. Zhang, S. Wang and J. Zheng, *J. Power Sources*, 2021, **499**, 229756.
110 H. J. Noh, S. Youn, C. S. Yoon and Y. K. Sun, *J. Power Sources*, 2013, **233**, 121–130.
111 Y. Kim, *J. Mater. Sci.*, 2013, **48**, 8547–8551.
112 S. H. Lee, G. J. Park, S. J. Sim, B. S. Jin and H. S. Kim, *J. Alloys Compd.*, 2019, **791**, 193–199.
113 D. H. Cho, C. H. Jo, W. Cho, Y. J. Kim, H. Yashiro, Y. K. Sun and S. T. Myung, *J. Electrochem. Soc.*, 2014, **161**, A920.
114 Z. Gan, G. Hu, Z. Peng, Y. Cao, H. Tong and K. Du, *Appl. Surf. Sci.*, 2019, **481**, 1228–1238.
115 H. J. Ban, M. Y. Kim, S. J. Park, B. S. Kang, J. Lim, Y. Hong, S. H. Yang and H. S. Kim, *Surf. Coat. Technol.*, 2022, **430**, 127984.
116 S. Dai, M. Yuan, L. Wang, L. Luo, Q. Chen, T. Xie, Y. Li and Y. Yang, *Ceram. Int.*, 2019, **45**, 674–680.
117 J. Huang, X. Fang, Y. Wu, L. Zhou, Y. Wang, Y. Jin, W. Dang, L. Wu, Z. Rong, X. Chen and X. Tang, *J. Electroanal. Chem.*, 2018, **823**, 359–367.
118 D. Becker, M. Börner, R. Nölle, M. Diehl, S. Klein, U. Rodehorst, R. Schmuch, M. Winter and T. Placke, *ACS Appl. Mater. Interfaces*, 2019, **11**, 18404–18414.
119 Y. Li, X. Li, J. Hu, W. Liu, H. Maleki Kheimeh Sari, D. Li, Q. Sun, L. Kou, Z. Tian, L. Shao, C. Zhang, J. Zhang and X. Sun, *Energy Environ. Mater.*, 2020, **3**, 522–528.
120 F. Ma, Y. Wu, G. Wei, S. Qiu and J. Qu, *J. Solid State Electrochem.*, 2019, **23**, 2213–2224.
121 X. Wang, J. Cai, Y. Liu, X. Han, Y. Ren, J. Li, Y. Liu and X. Meng, *Nanotechnology*, 2020, **32**, 115401.
122 X. Dai, A. Zhou, J. Xu, B. Yang, L. Wang and J. Li, *J. Power Sources*, 2015, **298**, 114–122.
123 D. Zhang, Y. Li, X. Xi, S. Wang, S. Hao, T. Lei, X. Ren, Y. Xiong, S. Liu and J. Zheng, *J. Alloys Compd.*, 2022, **906**, 164286.
124 Z. F. Tang, R. Wu, P. F. Huang, Q. S. Wang and C. H. Chen, *J. Alloys Compd.*, 2017, **693**, 1153–1163.
125 J. Ye, X. Zhai, L. Chen, W. Guo, T. Gu, Y. Shi, J. Hou, F. Han, Y. Liu, C. Fan, G. Wang, S. Peng and X. Guo, *J. Energy Chem.*, 2021, **62**, 252–261.

126 W. G. Ryu, H. S. Shin, M. S. Park, H. Kim, K. N. Jung and J. W. Lee, *Ceram. Int.*, 2019, **45**, 13942–13950.
127 H. Tong, P. Dong, J. Zhang, J. Zheng, W. Yu, K. Wei, B. Zhang, Z. Liu and D. Chu, *J. Alloys Compd.*, 2018, **764**, 44–50.
128 K. Park, J. H. Park, S. G. Hong, B. Choi, S. W. Seo, J. H. Park and K. Min, *Phys. Chem. Chem. Phys.*, 2016, **18**, 29076–29085.
129 F. Wang, Y. Luo, P. Liu, M. S. Balogun, J. Deng and Z. Wang, *Coatings*, 2022, **12**, 319.
130 D. Y. Hwang, H. S. Kim and S. H. Lee, *J. Mater. Chem. A*, 2022, **10**, 16555–16569.
131 T. Sattar, S. J. Sim, S. H. Lee, B. S. Jin and H. S. Kim, *Solid State Ionics*, 2022, **378**, 115886.
132 W. Li, L. Yang, Y. Li, Y. Chen, J. Guo, J. Zhu, H. Pan and X. Xi, *Front. Chem.*, 2020, **8**, 1–9.
133 Z. Zhao, S. Chen, D. Mu, R. Ma, C. Li, B. Wu, F. Wu, K. Cheng and C. Xie, *J. Power Sources*, 2019, **431**, 84–92.
134 H. Xie, Z. Liang, D. Luo, Y. Zhang, X. Ding, J. Cui, Z. Zhang and Z. Lin, *Chem. Commun.*, 2020, **56**, 12009–12012.
135 K. Sahni, M. Ashuri, Q. He, R. Sahore, I. D. Bloom, Y. Liu, J. A. Kaduk and L. L. Shaw, *Electrochim. Acta*, 2019, **301**, 8–22.
136 S. T. Myung, F. Maglia, K. J. Park, C. S. Yoon, P. Lamp, S. J. Kim and Y. K. Sun, *ACS Energy Lett.*, 2017, **2**, 196–223.
137 Y. Di Xu, W. Xiang, Z. G. Wu, C. L. Xu, Y. C. Li, X. D. Guo, G. P. Lv, X. Peng and B. H. Zhong, *Electrochim. Acta*, 2018, **268**, 358–365.
138 J.-Y. Liang, X.-X. Zeng, X.-D. Zhang, P.-F. Wang, J.-Y. Ma, Y.-X. Yin, X.-W. Wu, Y.-G. Guo and L.-J. Wan, *J. Am. Chem. Soc.*, 2018, **140**, 6767–6770.
139 X. M. Fan, Y. De Huang, H. X. Wei, L. B. Tang, Z. J. He, C. Yan, J. Mao, K. H. Dai and J. C. Zheng, *Adv. Funct. Mater.*, 2022, **32**, 2109421.
140 A. Y. Kim, F. Strauss, T. Bartsch, J. H. Teo, T. Hatsukade, A. Mazilkin, J. Janek, P. Hartmann and T. Brezesinski, *Chem. Mater.*, 2019, **31**, 9664–9672.
141 P. Oh, B. H. Song, W. D. Li and A. Manthiram, *J. Mater. Chem. A*, 2016, **4**, 5839–5841.
142 X. G. Sun, C. J. Jafta, S. S. Tan, A. Borisevich, R. B. Gupta and M. P. Paranthaman, *J. Electrochem. Soc.*, 2022, **169**, 020565.
143 S. S. Zhang, X. L. Fan and C. S. Wang, *Chemelectrochem*, 2019, **6**, 1536–1541.
144 B. Li, G. Li, D. Zhang, J. Fan, D. Chen, Y. Ge, F. Lin, C. Zheng and L. Li, *ChemistrySelect*, 2019, **4**, 6354–6360.
145 L. Song, F. Tang, Z. Xiao, Z. Cao, H. Zhu and A. Li, *J. Electron. Mater.*, 2018, **47**, 5896–5904.
146 A. Li, A. C. Y. Yuen, W. Wang, T. B. Y. Chen, C. S. Lai, W. Yang, W. Wu, Q. N. Chan, S. Kook and G. H. Yeoh, *Batteries*, 2022, **8**, 69.
147 S. Sun, J. Li, C. Xu, T. Zhai and H. Xia, *J. Mater. Chem. A*, 2022, **10**, 19231–19253.
148 Q. Liu, Z. Zhao, F. Wu, D. Mu, L. Wang and B. Wu, *Solid State Ionics*, 2019, **337**, 107–114.
149 T. Weigel, F. Schipper, E. M. Erickson, F. A. Susai, B. Markovsky and D. Aurbach, *ACS Energy Lett.*, 2019, **4**, 508–516.
150 Z. Huang, Z. Wang, H. Guo and X. Li, *J. Alloys Compd.*, 2016, **671**, 479–485.
151 L. Xue, Y. Li, B. Xu, Y. Chen, G. Cao, J. Li, S. Deng, Y. Chen and J. Chen, *J. Alloys Compd.*, 2018, **748**, 561–568.
152 Y. H. Chen, J. Zhang, Y. Li, Y. F. Zhang, S. P. Huang, W. Lin and W. K. Chen, *Phys. Chem. Chem. Phys.*, 2021, **23**, 11528–11537.
153 R. Zhang, H. Qiu and Y. Zhang, *Nanomaterials*, 2022, **12**, 729.
154 S. J. Do, P. Santhoshkumar, S. H. Kang, K. Prasanna, Y. N. Jo and C. W. Lee, *Ceram. Int.*, 2019, **45**, 6972–6977.
155 H. G. Park, K. Min and K. Park, *ACS Appl. Mater. Interfaces*, 2022, **14**, 5168–5176.
156 C. Wu, S. Cao, X. Xie, C. Guo, H. Li, Z. Li, Z. Zang, B. Chang, G. Chen, X. Guo, T. Wu and X. Wang, *Chem. Eng. J.*, 2022, **429**, 132141.
157 X. Huang, P. Zhang, Z. Liu, B. Ma, Y. Zhou and X. Tian, *ChemElectroChem*, 2022, **9**, e202100756.
158 L. Pan, Y. Xia, B. Qiu, H. Zhao, H. Guo, K. Jia, Q. Gu and Z. Liu, *J. Power Sources*, 2016, **327**, 273–280.
159 B. Li, H. Yan, J. Ma, P. Yu, D. Xia, W. Huang, W. Chu and Z. Wu, *Adv. Funct. Mater.*, 2014, **24**, 5112–5118.
160 S. Gao, X. Zhan and Y. T. Cheng, *J. Power Sources*, 2019, **410–411**, 45–52.
161 J. Shen, D. Deng, X. Li, B. Zhang, Z. Xiao, C. Hu, X. Yan and X. Ou, *J. Alloys Compd.*, 2022, **903**, 163999.
162 F. Reissig, M. A. Lange, L. Haneke, T. Placke, W. G. Zeier, M. Winter, R. Schmuch and A. Gomez-Martin, *ChemSusChem*, 2022, **15**, e202102220.
163 M. Nanthagopal, P. Santhoshkumar, N. Shaji, S. Praveen, H. S. Kang, C. Senthil and C. W. Lee, *Appl. Surf. Sci.*, 2019, **492**, 871–878.
164 Y. Lee, H. Kim, T. Yim, K. Y. Lee and W. Choi, *J. Power Sources*, 2018, **400**, 87–95.
165 L. Song, P. Jiang, Z. Xiao, Z. Cao, C. Zhou, J. Du and P. Liu, *Ionics*, 2021, **27**, 949–959.
166 M. A. Mezaal, L. Qu, G. Li, W. Liu, X. Zhao, Z. Fan and L. Lei, *J. Solid State Electrochem.*, 2017, **21**, 2219–2229.
167 Y. Jiang, Z. Liu, Y. Zhang, H. Hu, X. Teng, D. Wang, P. Gao and Y. Zhu, *Electrochim. Acta*, 2019, **309**, 74–85.
168 X. Xu, L. Xiang, L. Wang, J. Jian, C. Du, X. He, H. Huo, X. Cheng and G. Yin, *J. Mater. Chem. A*, 2019, **7**, 7728–7735.
169 Y. Mo, L. Guo, H. Jin, B. Du, B. Cao, Y. Chen, D. Li and Y. Chen, *J. Power Sources*, 2020, **468**, 228405.
170 P. Gao, S. Wang, Z. Liu, Y. Jiang, W. Zhou and Y. Zhu, *Solid State Ionics*, 2020, **357**, 115504.
171 C. Hua, K. Du, C. Tan, Z. Peng, Y. Cao and G. Hu, *J. Alloys Compd.*, 2014, **614**, 264–270.
172 Y. Li, R. Xu, Y. Ren, J. Lu, H. Wu, L. Wang, D. J. Miller, Y. K. Sun, K. Amine and Z. Chen, *Nano Energy*, 2016, **19**, 522–531.
173 J. Zhang, Z. Yang, R. Gao, L. Gu, Z. Hu and X. Liu, *ACS Appl. Mater. Interfaces*, 2017, **9**, 29794–29803.
174 Y. Zhang, H. Li, J. Liu, J. Zhang, F. Cheng and J. Chen, *J. Mater. Chem. A*, 2019, **7**, 20958–20964.

175 Y. K. Sun, Z. Chen, H. J. Noh, D. J. Lee, H. G. Jung, Y. Ren, S. Wang, C. S. Yoon, S. T. Myung and K. Amine, *Nat. Mater.*, 2012, **11**, 942–947.
176 Y. C. Li, W. Xiang, Y. Xiao, Z. G. Wu, C. L. Xu, W. Xu, Y. Di Xu, C. Wu, Z. G. Yang and X. D. Guo, *J. Power Sources*, 2019, **423**, 144–151.
177 F. Zhao, X. Li, Y. Yan, M. Su, L. Liang, P. Nie, L. Hou, L. Chang and C. Yuan, *J. Power Sources*, 2022, **524**, 231035.
178 J. Langdon and A. Manthiram, *Energy Storage Mater.*, 2021, **37**, 143–160.
179 S. Lu, L. Tang, H. Wei, Y. Huang, C. Yan, Z. He, Y.-j. Li, J. Mao, K. Dai and J.-c. Zheng, *Electrochem. Energy Rev.*, 2022, **5**, 15.
180 Y. Y. Qu, Y. Mo, X. B. Jia, L. Zhang, B. Du, Y. Lu, D. Lia and Y. Chen, *J. Alloys Compd.*, 2019, **788**, 810–818.
181 J. Zhu and G. Y. Chen, *J. Mater. Chem. A*, 2019, **7**, 5463–5474.
182 S. L. Spence, Z. Xu, S. Sainio, D. Nordlund and F. Lin, *Inorg. Chem.*, 2020, **59**, 10591–10603.
183 R. Liang, Z. Y. Wu, W. M. Yang, Z.-Q. Tang, G.-G. Xiong, Y. C. Cao, S.-R. Hu and Z. B. Wang, *Ionics*, 2020, **26**, 1635–1643.
184 T. Kimijima, N. Zettsu, K. Yubuta, K. Hirata, K. Kami and K. Teshim, *J. Mater. Chem. A*, 2016, **4**, 7289–7296.
185 X. L. Liu, J. J. Wu, X. L. Huang, Z. Liu, Y. Zhang, M. Wang and R. Che, *J. Mater. Chem. A*, 2014, **2**, 15200.
186 Y. Kim, *ACS Appl. Mater. Interfaces*, 2012, **4**, 2329–2333.
187 C. H. Lin, Y. Z. Zhang, L. Chen, Y. Lei, J. Ou, Y. Guo, H. Yuan and D. Xiao, *J. Power Sources*, 2015, **280**, 263–271.
188 D. Huang, Y. Shi, A. P. Tornheim, J. Bareño, Z. Chen, Z. C. Zhang, A. Burrell and H. Luo, *Appl. Mater. Today*, 2019, **16**, 342–350.
189 L. S. Zhang, H. Wang, L. Z. Wang and Y. Cao, *Appl. Surf. Sci.*, 2018, **450**, 461–467.
190 A. Ran, S. Chen, M. Cheng, Z. Liang, B. Li, G. Zhou, F. Kang, X. Zhang and G. Wei, *J. Mater. Chem. A*, 2022, **10**, 19680–19689.
191 M. Kim, J. Zhu, L. Li, C. Wang and G. Chen, *ACS Appl. Energy Mater.*, 2020, **3**, 12238–12245.
192 C. Liang, R. C. Longo, F. Kong, C. Zhang, Y. Nie, Y. Zheng and K. Cho, *ACS Appl. Mater. Interfaces*, 2018, **10**, 6673–6680.
193 Y. Lu, T. Zhu, E. McShane, B. D. McCloskey and G. Chen, *Small*, 2022, **18**, 2105833.
194 P. Teichert, H. Jahnke and E. Figgemeier, *J. Electrochem. Soc.*, 2021, **168**, 090532.
195 E. R. Logan, H. Hebecker, X. Ma, J. Quinn, Y. HyeJeong, S. Kumakura, J. Paulsen and J. R. Dahn, *J. Electrochem. Soc.*, 2020, **167**, 060530.
196 L. Saunders, J. Wang and U. Stimming, *J. Appl. Electrochem.*, 2022, **52**, 1305–1316.
197 H. Michael, R. E. Owen, J. B. Robinson, T. M. M. Heenan, C. Tan, A. J. Wade, R. Jervis, D. J. L. Brett and P. R. Shearing, *J. Power Sources*, 2022, **542**, 231775.
198 Q. Huang, L. Ma, A. Liu, X. Ma, J. Li, J. Wang and J. R. Dahn, *J. Power Sources*, 2018, **390**, 78–86.
199 G. Qian, Y. Zhang, L. Li, R. Zhang, J. Xu, Z. Cheng, S. Xie, H. Wang, Q. Rao, Y. He, Y. Shen, L. Chen, M. Tang and Z. F. Ma, *Energy Storage Mater.*, 2020, **27**, 140–149.
200 P. Pang, X. Tan, Z. Wang, Z. Cai, J. Nan, Z. Xing and H. Li, *Electrochim. Acta*, 2021, **365**, 137380.
201 C. Wang, R. Zhang, C. Siu, M. Ge, K. Kisslinger, Y. Shin and H. L. Xin, *Nano Lett.*, 2021, **21**, 9797–9804.
202 W. Jiang, X. Fan, X. Zhu, Z. Wu, Z. Li, R. Huang, S. Zhao, X. Zeng, G. Hu, B. Zhang, S. Zhang, L. Zhu, L. Yan, M. Ling, L. Wang and C. Liang, *J. Power Sources*, 2021, **508**, 230335.
203 H. Li, P. Zhou, F. Liu, H. Li, F. Cheng and J. Chen, *Chem. Sci.*, 2019, **10**, 1374–1379.
204 X. Zeng, J. Zhu, L. Yang, L. Zhou, L. Shao, S. Hu, C. Huan, C. Yang, D. Qian and X. Xi, *J. Electroanal. Chem.*, 2019, **838**, 94–100.
205 X. Zeng, T. Jian, Y. Lu, L. Yang, W. Ma, Y. Yang, J. Zhu, C. Huang, S. Dai and X. Xi, *ACS Sustainable Chem. Eng.*, 2020, **8**, 6293–6304.
206 A. M. Haregewoin, A. S. Wotango and B. J. Hwang, *Energy Environ. Sci.*, 2016, **9**, 1955–1988.
207 H. Lyu, Y. C. Li, C. J. Jafta, C. A. Bridges, H. M. Meyer, A. Borisevich, M. P. Paranthaman, S. Dai and X. G. Sun, *J. Power Sources*, 2019, **412**, 527–535.
208 W. Song, J. Harlow, E. Logan, H. Hebecker, M. Coon, L. Molino, M. Johnson, J. Dahn and M. Metzger, *J. Electrochem. Soc.*, 2021, **168**, 090503.
209 Y. Li, S. Wan, G. M. Veith, R. R. Unocic, M. P. Paranthaman, S. Dai and X. G. Sun, *Adv. Energy Mater.*, 2017, **7**, 1601397.
210 J. V. Laveda, J. E. Low, F. Pagani, E. Stilp, S. Dilger, V. Baran, M. Heere and C. Battaglia, *ACS Appl. Energy Mater.*, 2019, **2**, 7036–7044.
211 H. Liu, A. J. Naylor, A. S. Menon, W. R. Brant, K. Edström and R. Younesi, *Adv. Mater. Interfaces*, 2020, **7**, 2000277.
212 W. Zhao, L. Zou, J. Zheng, H. Jia, J. Song, M. H. Engelhard, C. Wang, W. Xu, Y. Yang and J. G. Zhang, *ChemSusChem*, 2018, **11**, 2211–2220.
213 S. Wen, Y. Han, P. Wang, D. Zhao, X. Cui, L. Zhang and S. Li, *ACS Appl. Energy Mater.*, 2021, **4**, 12525–12534.
214 K. Beltrop, S. Klein, R. Nolle, A. Wilken, J. J. Lee, T. K. J. Koster, J. Reiter, L. Tao, C. D. Liang, M. Winter, X. Qi and T. Placke, *Chem. Mater.*, 2018, **30**, 2726–2741.
215 Y. J. Qiu, D. S. Lu, Y. Y. Gai and Y. P. Cai, *ACS Appl. Mater. Interfaces*, 2022, **14**, 11398–11407.
216 Y. Zhu, Y. Li, M. Bettge and D. P. Abraham, *Electrochim. Acta*, 2013, **110**, 191–199.
217 S. Roser, A. Lerchen, L. Ibing, X. Cao, J. Kasnatscheew, F. Glorius, M. Winter and R. Wagner, *Chem. Mater.*, 2017, **29**, 7733–7739.
218 D. X. Ouyang, W. T. Song, K. Oh, K. W. Ahn, D. S. Hal, T. Hynes, J. Wang and J. Dahn, *J. Electrochem. Soc.*, 2022, **169**, 040565.
219 Y. Zheng, Y. Yao, J. Ou, M. Li, D. Luo, H. Dou, Z. Li, K. Amine, A. Yu and Z. Chen, *Chem. Soc. Rev.*, 2020, **49**, 8790–8839.
220 W. Jiang, X. Zhu, R. Huang, S. Zhao, X. Fan, M. Ling, C. Liang and L. Wang, *Adv. Energy Mater.*, 2022, **12**, 2103473.

221 S. Sun, C. Z. Zhao, H. Yuan, Y. Lu, J.-K. Hu, J.-Q. Huang and Q. Zhang, *Mater. Future*, 2022, **1**, 012101.
222 C. Roitzheim, Y. J. Sohn, L.-Y. Kuo, G. Häuschen, M. Mann, D. Sebold, M. Finsterbusch, P. Kaghazchi, O. Guillon and D. F. Rohlfing, *ACS Appl. Energy Mater.*, 2022, **5**, 6913–6926.
223 Y.-W. Song, K. Heo, D. Hwang, M.-Y. Kim, H. Le, B.-S. Kang, · Y. Hong, H. S. Kim, J. Kim and J. Lim, *Ionics*, 2022, **28**, 5421–5431.
224 L. W. Tian, J. W. Kim, S.-B. Hong, H.-H. Ryu, U.-H. Kim, Y.-K. Sun and D.-W. Kim, *Chem. Eng. J.*, 2022, **450**, 138043.
225 Z. Zhao, Z. Wen, X. Liu, H. Yang, S. Chen, C. Li, H. Lv, F. Wu, B. Wu and D. Mu, *Chem. Eng. J.*, 2021, **405**, 127031.
226 L. Chen, T. Gu, J. Ma, K. Yang, P. Shi, J. Biao, J. Mi, M. Liu, W. Lv and Y.-B. He, *Nano Energy*, 2022, **100**, 107470.
227 J.-P. Zeng, J.-F. Liu, H.-D. Huang, S.-C. Shi, B.-H. Kang, C. Dai, Li-W. Zhang, Z. C. Yan, F. J. Stadler, Y.-B. He and Y.-F. Huang, *J. Mater. Chem. A*, 2022, **10**, 18061–18069.
228 H.-Y. Zhou, S.-S. Yan, J. Li, H. Dong, P. Zhou, L. Wan, X.-X. Chen, W.-L. Zhang, Y.-C. Xia, P.-C. Wang, B.-G. Wang and K. Liu, *ACS Appl. Mater. Interfaces*, 2022, **14**, 24469–24479.
229 Q. Li, X. Zhang, J. Peng, Z. Wang, Z. Rao, Y. Li, Z. Li, C. Fang, J. Han and Y. Huang, *ACS Appl. Mater. Interfaces*, 2022, **14**, 21018–21027.
230 X. Li, W. Peng, R. Tiana, D. Song, Z. Wang, H. Zhang, L. Zhu and L. Zhang, *Electrochim. Acta*, 2020, **363**, 137185.
231 X. Liu, J. Shi, B. Zheng, Z. Chen, Y. Su, M. Zhang, C. Xie, M. Su and Y. Yang, *ACS Appl. Mater. Interfaces*, 2021, **13**, 41669–41679.
232 F. Zhang, S. Lou, S. Li, Z. Yu, Q. Liu, A. Dai, C. Cao, M. F. Toney, M. Ge, X. Xiao, W.-K. Lee, Y. Yao, J. Deng, T. Liu, Y. Tang, G. Yin, J. Lu, D. Su and J. Wang, *Nat. Commun.*, 2020, **11**, 3050.
233 F. Wu, G. T. Kim, M. Kuenzel, H. Zhang, J. Asenbauer, D. Geiger, U. Kaiser and S. Passerini, *Adv. Energy Mater.*, 2019, **9**, 1902445.
234 J. Lan, Q. Zheng, H. Zhou, J. Li, L. Xing, K. Xu, W. Fan, L. Yu and W. Li, *ACS Appl. Mater. Interfaces*, 2019, **11**, 28841.
235 F. Wu, G. T. Kim, T. Diemant, M. Kuenzel, A. R. Schür, X. Gao, B. Qin, D. Alwast, Z. Jusys and R. J. Behm, *Adv. Energy Mater.*, 2020, **10**, 2001830.
236 Z. Zhu, R. Gao, I. Waluyo, Y. Dong, A. Hunt, J. Lee and J. Li, *Adv. Energy Mater.*, 2020, **10**, 2001120.
237 J. G. Ren, Q. H. Wu, G. Hong, W. J. Zhang, H. Wu, K. Amine, J. Yang and S. T. Lee, *Energy Technol.*, 2013, **1**, 77.
238 A. Aishova, G. T. Park, C. S. Yoon and Y. K. Sun, *Adv. Energy Mater.*, 2020, **10**, 1903179.
239 W. Li, S. Lee and A. Manthiram, *Adv. Mater.*, 2020, **32**, 2002718.
240 T. Liu, L. Yu, J. Liu, J. Lu, X. Bi, A. Dai, M. Li, M. Li, Z. Hu and L. Ma, *Nat. Energy*, 2021, **6**, 277.
241 B. Aktekin, M. Valvo, R. I. Smith, M. H. Sørby, F. Lodi Marzano, W. Zipprich, D. Brandell, K. Edström and W. R. Brant, *ACS Appl. Energy Mater.*, 2019, **2**, 3323.
242 M. S. Milien, H. Beyer, W. Beichel, P. Klose, H. A. Gasteiger, B. L. Lucht and I. Krossing, *J. Electrochem. Soc.*, 2018, **165**, A2569.
243 A. Hofmann, A. Höweling, N. Bohn, M. Müller, J. R. Binder and T. Hanemann, *ChemElectroChem*, 2019, **6**, 5255.
244 G. Pagot, M. Bandiera, K. Vezz` u, A. Migliori, R. Bertoncello, E. Negro, V. Morandi and V. D. Noto, *J. Mater. Chem. A*, 2020, **8**, 25727–25738.